

Article

Multiscale Computational Simulation of Amorphous Silicates' Structural, Dielectric, and Vibrational Spectroscopic Properties

José Ángel Martínez-González ^{1,2} , Javier Navarro-Ruiz ^{1,3}  and Albert Rimola ^{1,*}

¹ Departament de Química, Universitat Autònoma de Barcelona, 08193 Bellaterra, Republic of Catalonia, Spain; jose.martinez-gonzalez@stfc.ac.uk (J.Á.M.-G.); jnavarro@iciq.es (J.N.-R.)

² Isis Neutron and Muon Source, STFC Rutherford Appleton Laboratory, Harwell Science and Innovation Campus, Didcot, OX11 0QX, UK

³ Institute of Chemical Research of Catalonia, ICIQ, and The Barcelona Institute of Science and Technology, BIST, Av. Països Catalans 16, 43007 Tarragona, Spain

* Correspondence: albert.rimola@uab.cat; Tel.: +34-935-812-164

Received: 25 June 2018; Accepted: 7 August 2018; Published: 15 August 2018



Abstract: Silicates are among the most abundant and important inorganic materials, not only in the Earth's crust, but also in the interstellar medium in the form of micro/nanoparticles or embedded in the matrices of comets, meteorites, and other asteroidal bodies. Although the crystalline phases of silicates are indeed present in nature, amorphous forms are also highly abundant. Here, we report a theoretical investigation of the structural, dielectric, and vibrational properties of the amorphous bulk for forsterite (Mg_2SiO_4) as a silicate test case by a combined approach of classical molecular dynamics (MD) simulations for structure evolution and periodic quantum mechanical Density Functional Theory (DFT) calculations for electronic structure analysis. Using classical MD based on an empirical partial charge rigid ionic model within a melt-quenching scheme at different temperatures performed with the GULP 4.0 code, amorphous bulk structures for Mg_2SiO_4 were generated using the crystalline phase as the initial guess. This has been done for bulk structures with three different unit cell sizes, adopting a super-cell approach; that is, $1 \times 1 \times 2$, $2 \times 1 \times 2$, and $2 \times 2 \times 2$. The radial distribution functions indicated a good degree of amorphization of the structures. Periodic B3LYP-geometry optimizations performed with the CRYSTAL14 code on the generated amorphous systems were used to analyze their structure; to calculate their high-frequency dielectric constants (ϵ_∞); and to simulate their IR, Raman, and reflectance spectra, which were compared with the experimental and theoretical crystalline Mg_2SiO_4 . The most significant changes of the physicochemical properties of the amorphous systems compared to the crystalline ones are presented and discussed (e.g., larger deviations in the bond distances and angles, broadening of the IR bands, etc.), which are consistent with their disordered nature. It is also shown that by increasing the unit cell size, the bulk structures present a larger degree of amorphization.

Keywords: DFT; periodic simulations; amorphous minerals; physicochemical properties; super-cell

1. Introduction

Amorphous materials are disordered solid-state systems that present a lack of long-range order, and from a thermodynamic standpoint, they are less stable than the corresponding crystalline structures. As a consequence of this long-range structural disorganization, amorphous materials usually exhibit different properties with respect to their crystalline counterparts. This is the case, for instance, for silica [1]. Whereas crystalline silica presents cytotoxicity when in contact with cellular systems [2–5], amorphous silica particles show high levels of biocompatibility [6], thus allowing them to be used in bioglass-based

implants [7] and as drug delivery systems [8]. In other cases, because of the different physicochemical properties between the crystalline and the amorphous partners, the amorphous phases are preferable to be used in semiconductor devices, such as the case of HfO_2 and ZrO_2 and their alloys [9–11].

The understanding and the prediction of the physicochemical properties of noncrystalline solids rely on the proper description of their structure at the atomic level. Experimental techniques with this purpose are X-ray and neutron diffraction, which are directly sensitive to the structure, and also vibrational-related spectroscopies such as infrared (IR) and Raman, in which detailed structural information can be achieved. However, an atomic-level understanding of amorphous materials derived from these experimental methods has so far remained elusive, in part because of the limited capabilities of the instrumentation for direct characterization. For instance, crystalline silicates exhibit a wealth of narrow IR bands [12,13], whereas for amorphous silicates, these bands result in a significant broadening and blending due to the wide range of bond lengths and angles characteristic of the amorphous nature [14–16]. Thus, deriving detailed structural information by means of these experimental techniques is a daunting task. A complimentary tool with which to obtain atomistic details of the structure of amorphous systems and their relationships with their physicochemical features such as spectral signatures is the theoretical modeling approach. However, in contrast to crystalline systems, theoretical studies of the structure of amorphous materials are quite limited, probably because of the difficulty in generating realistic and reliable structural models with the available theoretical methods [17,18]. Among the different strategies to generate bulk amorphous structures, the melt-and-quench scheme has successfully been used to simulate different amorphous oxides [10,18–26]. This scheme consists of performing molecular dynamics (MD) simulations, taking the crystalline bulks as the initial guess and submitting them to a series of heating/cooling cycles. The heating at high temperatures followed by rapid cooling allows the sampling of the large configurational spaces and ensures a good degree of amorphization of the initial crystalline systems. However, the simulation of amorphous structures typically requires systems with more than 100 atoms per unit cell. Accordingly, despite the enormous growth in computational power, generating highly disordered materials adopting the melt-and-quench scheme approach by means of first-principles MD simulations are often prohibitively expensive, so the simulation timescales are limited to several picoseconds, which are relatively short in terms of the time frame for evolution into the amorphous structures. As an alternative, classical force field MD simulations are computationally less expensive, thus allowing larger timescales of up to several hundred picoseconds. By contrast, these classical MD simulations require accurate and reliable interatomic potentials, since the results are biased by the employed force fields. Proceeding this way, first-principles calculations onto the generated structural models are subsequently mandatory if the electronic structure and spectroscopic properties are desired.

Silicate-based materials constitute ca. 95 percent of the rocks of the Earth's crust [27]. Silicates are inorganic materials whose main feature is the orthosilicate $[\text{SiO}_4]^{4-}$ building block. The negative net electrical charge is compensated by metal cations. The ways how the different tetrahedral $[\text{SiO}_4]^{4-}$ units are linked (i.e., sharing corners, edges, and faces) and the nature of the counteractions give rise to the wide class of silicate structures. The wide presence of silicates is not only limited to the Earth's crust; they are also major components of the solid matter present in the universe, comprising a part of interstellar, circumstellar, and interplanetary dust particles; comets; and meteorites [28–30]. The most astrophysically important silicate groups are olivines and pyroxenes, with the preponderance of Mg^{2+} and Fe^{2+} as counteractions, since they appear with the highest cosmic abundance. Olivines are characterized to have the $[\text{SiO}_4]^{4-}$ tetrahedra linked by Mg^{2+} and Fe^{2+} and the general formula $\text{Mg}_{2x}\text{Fe}_{(2-2x)}\text{SiO}_4$ ($x = 0-1$), with the two end members named forsterite (Mg_2SiO_4) and fayalite (Fe_2SiO_4); whereas pyroxenes are formed by single chains of $[\text{SiO}_4]^{4-}$ intercalated by the divalent cations and have the general formula $\text{Mg}_x\text{Fe}_{(1-x)}\text{SiO}_3$ ($x = 0-1$), with the two end members named enstatite (MgSiO_3) and ferrosilite (FeSiO_3). In contrast to the terrestrial silicates, cosmic silicates are mainly found in an amorphous state [28,31], probably due to their exposure with various processes during their life cycle such as incident cosmic rays and UV radiation, thermal shocks,

or sputtering/shattering effects. Cosmic silicates play a significant role in the chemical evolution occurring in space as they provide the surfaces where important chemical reactions can take place, such as the formation of H_2 [32] and H_2O [33,34]. On the other hand, both crystalline and amorphous silicates can be synthesized, with special efforts regarding forsterite. Synthetic crystalline forsterite was achieved for the first time by Shankland and coworkers [35] using the Verneuil flame fusion method for the solid-state reaction between powders of MgO and SiO_2 . However, the crystals contained inclusions of unreacted MgO . Accordingly, this procedure has been improved (e.g., [36,37]) or modified (e.g., by mixing bauxite with $MgCO_3$ [38]), and alternative methods with enhanced qualities of the synthesized crystals have appeared, such as various sol-gel methods [39–41] and the application of modified Czochralski-pulling procedures; the latter providing large high-quality forsterite single nanocrystals [42–44]. Amorphous phases of forsterite can be synthesized by a variety of techniques: standard melt-and-quench methods [45–47], sol-gel reactions [48], sputtering techniques [49], and via energetic processing of the starting materials such as shocks [50] or collisions [51,52]. To produce amorphous silicate interstellar dust analogues, the processing of crystalline forsterite is usually performed [53–55]. The synthesized materials are characterized by standard solid-state techniques. X-ray diffraction (XRD) is useful to assess the degree of crystallinity and to analyze the phase purity in crystalline samples [56–58]. X-ray absorption spectroscopy (XAS), including extended X-ray absorption fine structure (EXAFS) and X-ray absorption near edge structure (XANES), is an analytical technique to determine short- and medium-range order in partially amorphous forsterite samples. This technique has been useful to determine that bond lengths and angles within the SiO_4 tetrahedra are not affected by the structural state [48]. Infrared-based spectroscopy is also useful to characterize the structural state, since crystalline forsterite presents a group of sharp bands in the $200\text{--}1000\text{ cm}^{-1}$ range [59,60], while amorphous phases present essentially two broad bands centered at about 1000 and 500 cm^{-1} [61]. Scanning electronic microscopy (SEM) is used to analyze the surface morphology of forsterite powders, which can be diverse (e.g., spherical, chain-like, porous, dendritic, etc.) depending on the experimental preparation [56,62], while transmission electron microscopy (TEM) provides direct imaging of parts of the forsterite nanoparticle samples, thus allowing the measuring of their composition, shape, size, and the atomic arrangement [63–65]. Synthesized forsterite nanoparticles have potential applications in enhanced weathering, namely sequestering CO_2 by mineral reactions [66–70], and as a biomaterial for implants [71–75]. Moreover, doping the forsterite nanomaterials with Eu^{3+} , Tb^{3+} , or Er^{3+} induces enhancement of their photoluminescence properties [76–78], rendering them to have applications in optoelectronic devices.

The present work focuses on the theoretical modelling and electronic structure study of amorphous Mg_2SiO_4 . Here, we combine classical MD simulations adopting the melt-and-quench scheme, for structural model generation, and DFT-based quantum mechanical (QM) calculations, for electronic structure analysis, to theoretically characterize the structural, dielectric, and spectroscopic properties of different amorphous silicate systems. Detailed analysis of the amorphous structures is carried out, including the coordination number and the radial distribution function of the systems. Geometry relaxations followed by calculation of the vibrational modes of the amorphous structural models serve to simulate the corresponding IR, Raman, and reflectance spectra at the B3LYP density functional level of theory by means of the periodic CRYSTAL14 *ab initio* code [79], which in turn are compared with the corresponding crystalline systems and the available experimental data. The presented results will be of great significance in the field of silicate chemistry. First, by matching the *ab initio* results with the experimental data, relationships between silicate spectral signatures and their atomistic structural details can be elucidated, which will be particularly useful for current and future astronomical archives (i.e., ALMA and the James Webb Space Telescope) and for the analysis of forthcoming results. Results will also be of importance for those studies devoted to the characterization of the spectroscopic properties of doped and/or modified forsterite nanomaterials, since we provide the reference spectroscopic properties of pure forsterite in both the crystalline and amorphous structural state. Finally, the work can also have repercussions from a computational point

of view. Generating the bulk structure of forsterite in an amorphous state is the first step towards obtaining the surface slab models for the same material. Having reliable slab models is of great importance since it is the basis upon which to subsequently carry out surface chemical studies, such as adsorption phenomena and heterogeneous catalytic reactivity. Finally, our results will be very useful to improve the force field parameters devoted to simulating the structure of silicates in an amorphous state. Only reliable parameters for crystalline silicates are available hitherto, so the present results can be used as a benchmark for the parametrization and to assess the accuracy of the force field, both in the simulation of the structure as well as in the prediction of the solid-state properties.

2. Computational Methods

2.1. Classical Molecular Dynamics (MD) Simulations

The procedure to generate the amorphous silicate models is inspired by that done for simulated bioglasses [18,19,21]. All models were generated by means of classical molecular dynamics simulations using the atomistic Born model of solids [80] implemented in the General Utility Lattice program (GULP) [81]. This model represents all ions as point charges interacting through Coulomb forces. Pairwise Buckingham potentials were used to represent Pauli repulsion and dispersion interactions, and the polarization of oxygen was represented by the shell model. All the interatomic potential parameters used in this work are shown in Table 1, which were derived from these references [82–84]. Moreover, the bulk structure of the crystalline Mg_2SiO_4 system calculated with GULP using these parameters is in very good agreement with the experimental one (see Figure S1 and Table S1, Supplementary Materials). The classical molecular dynamics (MD) simulations were carried out within the (N,V,T) canonical ensemble. The leapfrog Verlet algorithm was adopted using an integration time-step of 1 fs. The velocity rescaling scheme was used to control the temperature. Although the pressure was not directly equilibrated, we controlled the pressure of the system along all the simulations and we did not detect any dramatic change in the pressure that could cause a warning alert or stop the execution of the simulations.

- (1) Nose–Hoover thermostat. A total of 17 different final temperatures were considered, between 400 K and 2000 K, separated by 100 K each. It is worth mentioning that higher temperatures than the melting point of Mg_2SiO_4 (at about 1800 K) would have been desirable to accelerate the dynamics of the melting. However, we found that with MD simulations at these temperatures (e.g., 2500 K), the system was unstable because the interatomic potential parameters fail. After the heating process, classical MD simulations at the (N,V,T) ensemble at the given temperature were performed, which consisted of a 100 ps equilibration phase and a 200 ps production phase.
- (2) Cooling phase: After the production phase of the previous step, the resulting systems were subjected to MD simulations where the temperature was decreased by 0.005 K every time-step to reach the temperature of 300 K. At this temperature, the systems were equilibrated for 50 ps.
- (3) Second thermal/production phase: The structures obtained after the cooling simulations were then heated again to the temperature chosen in the first step. Then, MD simulations with an equilibration phase of 100 ps and a production phase of 200 ps production were performed.

Table 1. Classical potential parameters used in this study. Sub-index c and s have been used to refer to the core and shell of the atoms.

Charges			
Ions	Core	Shell	Core-shell interactions (eV Å ⁻²)
Mg	+2.00000		
Si	+4.00000		
O	+0.84819	−2.84819	74.92
Buckingham Potential	A (eV)	ρ (Å)	C (eV Å ⁶)
Mg _c –O _s	1428.500	0.31813	0.00000
Si _c –O _s	1283.907	0.32052	10.66158
O _c –O _s	22,764.300	0.14900	27.88000
Three-Body Potential	k (eV rad ⁻²)	Θ ₀ (degree)	
O _s –Si _c –O _s	2.097240	109.47000	

2.2. Quantum Mechanical (QM) Calculations

The resulting amorphous structures generated by the classical MD simulations were then optimized by means of periodic quantum mechanical calculations. To this end, simulations carried out with the CRYSTAL14 code [79] were performed, in which the crystalline orbitals representing the multielectron wave function are expressed by localized Gaussian-type orbitals (GTO). The following GTO basis set contractions were used: oxygen, (8s)–(411sp)–(1d); magnesium, (8s)–(511sp)–(1d); and silicon, (8s)–(6311sp)–(1d).

Self-Consistent Field (SCF) calculations and geometry optimizations were carried out using the hybrid B3LYP [85,86] DFT-based method. No symmetry was imposed during the geometry optimizations (i.e., P1 group symmetry), to enforce the maximum degrees of freedom in the optimization process. Both internal coordinates and lattice constants were optimized, using the Broyden–Fletcher–Goldfarb–Shanno (BFGS) algorithm [87]. All these technical details have already been used for the simulation of crystalline forsterite [88–90] and fayalite [91] bulk properties. Additional calculations have been done at B3LYP-D2, adopting the scheme proposed by Grimme [92] to include dispersion interactions and to check if they are of significance in the geometry optimization. Results (shown in Tables S1 and S2, Supplementary Materials) indicate that the inclusion of dispersion is, in practice, negligible; it systematically slightly reduces the internal bond lengths and the lattice distances compared to the pure B3LYP values, which in some cases (e.g., Mg–O distances), are shorter than the experimental values.

For the tolerances controlling the Coulomb and exchange series, the default values have been adopted; namely, (6 6) and (6 6 16), respectively. Accordingly, when the overlap between two atomic orbitals is smaller than 10⁻⁶ (for Coulomb) and 10⁻¹⁶ (for exchange), the integral is disregarded. The Brillouin zone is sampled by diagonalizing the Hamiltonian matrix in 63 reciprocal lattice points (*k* points), which corresponds to a shrinking factor of 5 [93]. The unrestricted formalism was adopted for the open-shell calculations.

Vibrational frequencies of the systems under study have been obtained as the eigenvalues of the diagonalized mass-weighted Hessian matrix considering the Γ point (i.e., the central zone, point *k* = 0 in the first Brillouin zone). The mass-weighted Hessian matrix was calculated via numerical differentiation of the analytical first energy derivatives, in which each 3N equilibrium nuclear coordinate was displaced by 0.003 Å. More details of the computational conditions and other numerical aspects concerning the calculation of the vibrational frequencies can be found in [94]. The infrared intensities were computed with the variation of the dipole moment along each normal mode, using, in this case, localized Wannier functions [95–97], whereas Raman intensities were calculated analytically through the coupled-perturbed Hartree-Fock (CPHF) scheme implemented in CRYSTAL [98,99] and successfully performed for different crystalline minerals [100–108]. The

reflectance spectra ($R(\nu)$) were simulated by first calculating different properties: (i) the vibrational frequencies, the corresponding intensities, and separation of the longitudinal and transverse optical modes [94,109]; (ii) the high-frequency dielectric tensor (ϵ_∞) [101,103,105,108], which contributes to the frequency-dependent complex dielectric function ($\epsilon(\nu)$) [98,99,110,111]; and (iii) the mass-weighted effective mode Born charges [112–114]. By combining all these ingredients, the reflectance spectra of several crystalline mineral systems have successfully been simulated [88,89,91,115–117].

3. Results and Discussion

This section is organized as follows. The first part addresses the generation of an amorphous bulk structure of forsterite (Mg_2SiO_4) by means of classical MD simulations and subsequent optimization at a quantum chemical level. A structural analysis of the optimized structure is presented, and investigations on its dielectric and vibrational properties by calculating the high-frequency dielectric constants and simulating the infrared, Raman, and reflectance spectra are shown, which in turn are compared with the experimental and theoretical crystalline Mg_2SiO_4 data. The second part is focused on the influence of the unit cell size of the amorphous Mg_2SiO_4 bulk on the structural, dielectric, and vibrational properties.

3.1. The Amorphous $1 \times 1 \times 2$ Super-Cell Mg_2SiO_4 System

As mentioned in Computational Methods, the initial guess used to generate the amorphous Mg_2SiO_4 bulk structure (hereafter referred to as Fo) was the Mg_2SiO_4 crystalline system. The bulk crystal structure of Mg_2SiO_4 consists of distorted SiO_4 and MgO_6 units that share their vertices (see Figure 1). Two symmetry-independent Mg atoms (referred to as Mg1 and Mg2 in Figure 1) are present in the crystal system. The Mg1-centered octahedra share edges, forming rods parallel to the crystallographic c axis, while the Mg2-centered octahedra link these rods through their edges (see Figure 1).

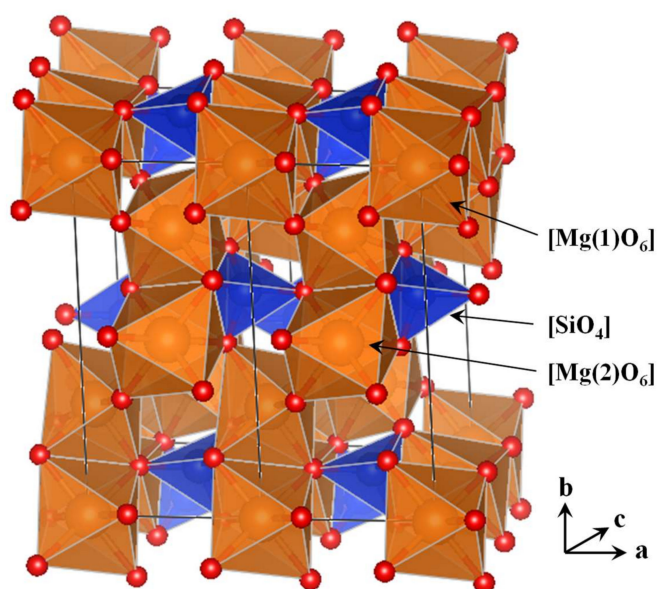


Figure 1. View (along the c crystallographic axis) of the crystal structure of forsterite. The two symmetry-independent Mg atoms are indicated according to the octahedral units $[\text{Mg}(1)\text{O}_6]$ and $[\text{Mg}(2)\text{O}_6]$ (in brown). The tetrahedral $[\text{SiO}_4]$ unit blocks (in blue) are also indicated. O atoms are shown in red.

Classical MD simulations at different temperatures adopting the procedure described in Computational Methods were executed to amorphize the structure of crystalline Mg_2SiO_4 . As the

primitive unit cell is small (*Pbnm* space symmetry with lattice parameters of $a = 4.79 \text{ \AA}$, $b = 10.19 \text{ \AA}$, and $c = 5.85 \text{ \AA}$), in this part, a larger unit cell has been adopted by doubling the c lattice parameter to favor an easier amorphization of the structure (hereafter referred to as $1 \times 1 \times 2$). In the next section, a detailed analysis of the effect of the unit cell size on the physicochemical properties of the amorphous structures is presented. Figure 2 shows the resulting structures at the end of the simulations run at the different temperatures. As one can see, the initial crystallinity becomes lost when increasing the temperatures. Figure 3 shows the pair correlation functions, $g(r)$, for the Mg atoms with either the neighboring Mg atoms (a, Mg–Mg) or the O atoms (b, Mg–O), derived from the simulations at $T = 300, 700, 900, 1200, 1500,$ and 1800 K . It is worth mentioning that the $g(r)$ curves should tend to 1 at long ranges. However, due to the relatively small size of the unit cell, if we account for the periodic boundary conditions (PBC), $g(r)$ curves are limited to ca. 3.5 \AA , hampering us in providing significant information. These $g(r)$ curves are shown in Figure S2 (Supplementary Materials). Therefore, in order to extend the $g(r)$ curves beyond the limits of the unit cell, we did not consider the PBC and hence, the $g(r)$ curves are not forced to tend to 1. In our particular case, they tend to 0 as a consequence of the absence of replica images (i.e., equivalent atomic positions) when the pair correlation functions were calculated. At 300 K , the $g(r)$ functions first present a sharp peak, followed by a subset of lower well-defined peaks, in agreement with the crystalline nature of Fo at this temperature. The first peak is representative of the Mg–Mg and Mg–O lengths of the first shell, while the others represent the distribution of the Mg–Mg and Mg–O distances of the outer shells. An increase of the temperature produces a broader profile of $g(r)$, in which the first peak significantly loses intensity, while the others overlap each other up to a point where at high temperatures, only two broad peaks are appreciable. These changes clearly indicate that a progressive loss of crystallinity occurs upon temperature increase.

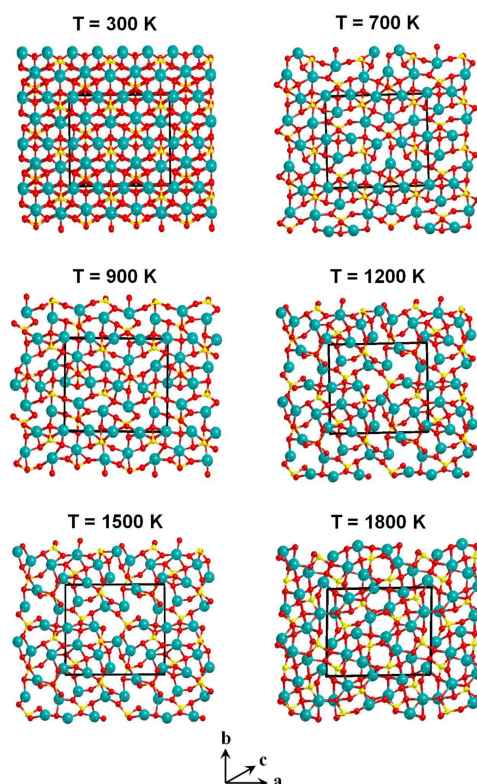


Figure 2. Structures obtained by classical molecular dynamics (MD) simulations. For all simulations, the initial guess structure was the crystal system. It was initially heated up to the given temperature and then submitted to the MD simulations at the (N,V,T) ensemble. Unit cells are shown in black. Mg atoms in green, Si atoms in yellow and O atoms in red.

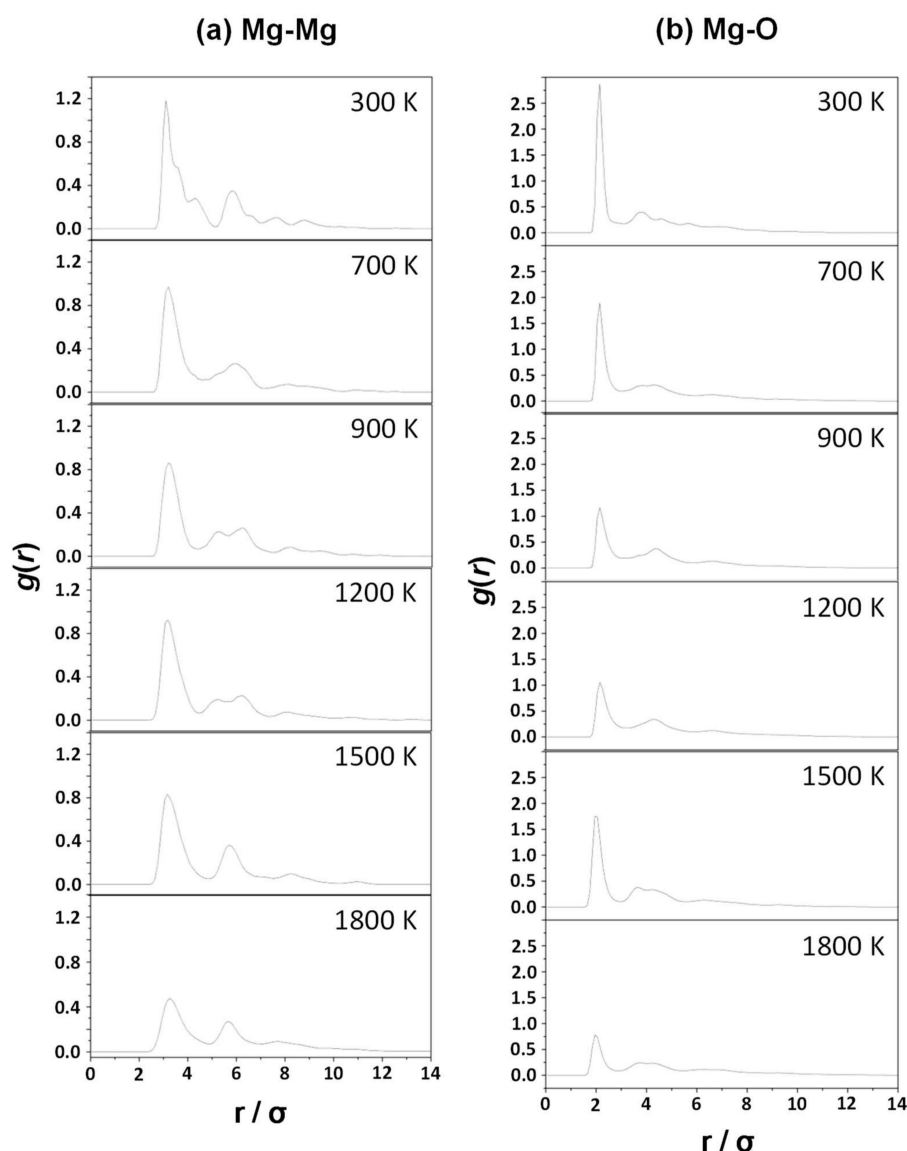


Figure 3. Mg–Mg (a) and Mg–O (b) pair correlation functions, $g(r)$, derived from the MD simulations at the different temperatures.

As the structure generated at $T = 1800$ K is the most disordered one, this was chosen for study of the structural and vibrational properties at the DFT level. Figure 4 shows the initial (crystalline) and the final (amorphous) structures optimized at the B3LYP theory level. It is also worth mentioning that those structures generated between 400 and 1600 K collapsed onto the crystal system upon optimization, whereas those between 1700 and 2000 K remained as amorphous structures. Table 2 shows the B3LYP-optimized lattice parameters and the range of the calculated Mg–O and Si–O bond lengths of amorphous Fo, as well as the volume and the density. For comparison, Table 2 also presents the same parameters for Fo crystal (experimental and calculated). In addition to the systematic larger values obtained by the calculated values for the crystal system, results indicate that the range of values of the amorphous system is larger than the crystal ones. This is indicative that the B3LYP-optimized amorphous Fo presents a larger distribution of bond lengths characteristic of the amorphous materials. It is worth mentioning that due to the disorganization of the internal atomic positions in the amorphous Fo, classifying the Mg atoms as Mg1 and Mg2 is not possible. The cell parameters of the amorphous Fo experiencing more variation compared to the crystalline values are a and b ; that is, a is about 0.2 Å

larger, while b is 0.8 Å shorter. Calculated lattice angles are also somewhat different, and essentially deviate from the ideal 90 degrees. Because of the significant shortening of the b cell parameter, the volume of the amorphous Fo is smaller than the crystal volumes. The fact that the density of the crystalline systems is lower than the amorphous one is also indicative of the amorphization of the system. Bearing in mind that amorphous materials are characterized by a random structure and poor order, giving rise to the presence of porosity.

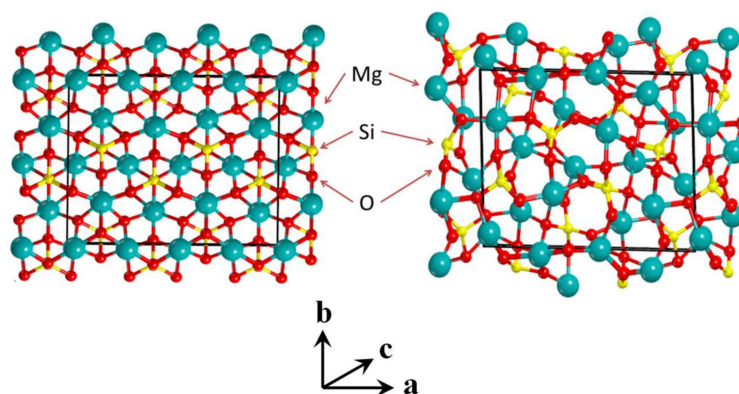


Figure 4. B3LYP-optimized structures of Mg_2SiO_4 bulk structure in the crystal form (left) and in an amorphous form (right) generated by classical MD simulations at $T = 1800$ K. Unit cells are shown in black.

Table 2. Bond distance ranges and cell parameters of the Mg_2SiO_4 bulk structures: experimental values of the crystal system as well as B3LYP-optimized values of the crystal and amorphous systems. The calculated volume and densities derived from the B3LYP-optimized geometries are also shown.

	Experimental	Crystal	Amorphous
Si–O (Å)	1.616–1.649	1.628–1.673	1.618–1.693
Mg1–O (Å)	2.069–2.126	2.073–2.131	1.929–2.226
Mg2–O (Å)	2.040–2.166	2.062–2.222	
a (Å)	4.746	4.789	4.93
b (Å)	10.18	10.25	9.37
c (Å)	5.976	6.009	5.97 (11.94) ¹
α (degrees)	90.0	90.0	87.4
β (degrees)	90.0	90.0	90.6
γ (degrees)	90.0	90.0	88.6
Volume (Å ³)	288.73	295.10	275.78 (551.00) ¹
Density (g·cm ^{−3})	3.22	3.34	3.37

¹ Because of the enlargement of the unit cell along the c axis (see text), for a proper comparison, bare values were derived from the actual calculated values (values in parenthesis).

In order to understand the nature of the amorphization of the silicate material, the deviation of the internal O–Si–O and O–Mg–O angles of the optimized system with respect to the ideal values is examined (reported in Table 3). These values reveal that the O–Mg–O angle presents the largest deviation ($\approx 15.3\%$), and therefore, the distortion of these angles contributes significantly to the amorphous nature. However, the deviation of the O–Si–O angle is not insubstantial ($\approx 6.5\%$), although the distortion of these angles also contributes by some amount to the internal atomic disorder.

The high-frequency dielectric constants (ϵ_∞) were also calculated using the CPKS scheme implemented in the CRYSTAL code. Results are shown in Table 4, in which the ϵ_∞ values along the x , y , and z directions of the amorphous Fo are compared with the experimental and calculated ones for Fo crystal. For the crystal systems, ϵ_∞ is notably symmetrical, the values slightly differing as a function of the direction; that is, both the experimental [118] and calculated values give $\epsilon_{\infty,x}$ as the

largest value, yet $\epsilon_{\infty,y}$ as the smallest, with a difference of 0.12–0.15 units. In contrast, for amorphous Fo, the difference between the largest and the smallest ϵ_{∞} values, which now correspond to $\epsilon_{\infty,x}$ and $\epsilon_{\infty,z}$, respectively, is a meager 0.07 units. This is consistent with the disordered nature of amorphous Fo, since the direction dependency of ϵ_{∞} typical of crystalline systems is partially lost.

Table 3. Mean values and the corresponding average deviations (with respect to the ideal value) of the O–Si–O and O–Mg–O angles of the optimized amorphous $1 \times 1 \times 2$, $2 \times 1 \times 2$, and $2 \times 2 \times 2$ Mg₂SiO₄ systems.

Angle (Degrees)	Ideal Value	Mean Value \pm Standard Deviation (Average Deviation)		
		$1 \times 1 \times 2$	$2 \times 1 \times 2$	$2 \times 2 \times 2$
O–Si–O	110.0	109.5 \pm 7.2(6.53%)	108.9 \pm 12.4(11.3%)	104.9 \pm 12.8(11.6%)
O–Mg–O	90.0	94.7 \pm 13.8(15.3%)	100.9 \pm 22.1(24.6%)	104.1 \pm 16.5(18.3%)

Table 4. High-frequency dielectric constants (ϵ_{∞}) for the Mg₂SiO₄ bulk structures along the *x*, *y*, and *z* directions: experimental values of the crystal system and B3LYP-optimized values of the crystal and amorphous systems.

	Experimental ¹	Crystal	Amorphous
$\epsilon_{\infty,x}$	2.789	2.571	2.284
$\epsilon_{\infty,y}$	2.673	2.424	2.247
$\epsilon_{\infty,z}$	2.726	2.475	2.218

¹ From reference [118].

Crystalline Fo has an orthorhombic structure. It presents 28 atoms in the unit cell (six symmetry-independent atoms), which give rise to four formula units per cell. Its symmetry decomposition corresponds to $\Gamma_{\text{total}} = 11A_g + 11B_{1g} + 7B_{2g} + 7B_{3g} + 10A_u + 10B_{1u} + 14B_{2u} + 14B_{3u}$, in which the three B_{1u} , B_{2u} , and B_{3u} correspond to rigid transitions and the remaining modes are the vibrational and rotational modes that can be classified as: 35 IR-active modes ($9B_{1u} + 13B_{2u} + 13B_{3u}$), 36 Raman-active modes ($11A_g + 11B_{1g} + 7B_{2g} + 7B_{3g}$), and 10 A_u inactive modes. In previous works, mode classification and band assignments of crystalline Fo have exhaustively been discussed by means of infrared, Raman, and reflectance spectroscopic measurements [12,59,60,119–124]. In this part, we focus our attention on the most important changes due to the amorphization of the crystal system. Figure 5 shows the B3LYP-simulated IR spectrum of amorphous Fo, where for comparison, the B3LYP-simulated and the experimental IR spectra for the crystal systems are also shown. The simulated spectra were broadened by Lorentzian functions with a typical width of $\delta\nu = 20 \text{ cm}^{-1}$, which is comparable with the bandwidth of experimental IR spectrum. For crystal Fo, the experimental and theoretical vibrational IR and Raman spectra compare fairly well. In the IR case, both spectra present a wealth of narrow bands in agreement with their crystalline nature. As already described by some of us and by other colleagues, B3LYP frequencies reproduce the experimental IR values very well (for more details, see [90,125]). Figure 6 shows the B3LYP-simulated Raman spectrum of amorphous and crystal Fo, and Table 5 reports the calculated Raman-active frequencies (classified by their symmetries) with the corresponding intensity of the crystalline system, which are compared with those measured experimentally (including frequency deviations). In the Raman case, B3LYP reproduces the experimental Raman data quite well, with a mean average deviation of 24.9–34.6 cm^{-1} and a largest deviation of 81–82 cm^{-1} . Remarkably, for the calculated two most intense Raman peaks (i.e., at 848 and 883 cm^{-1}), the deviations compared to the corresponding experimental values are 27 and 22–24 cm^{-1} , respectively.

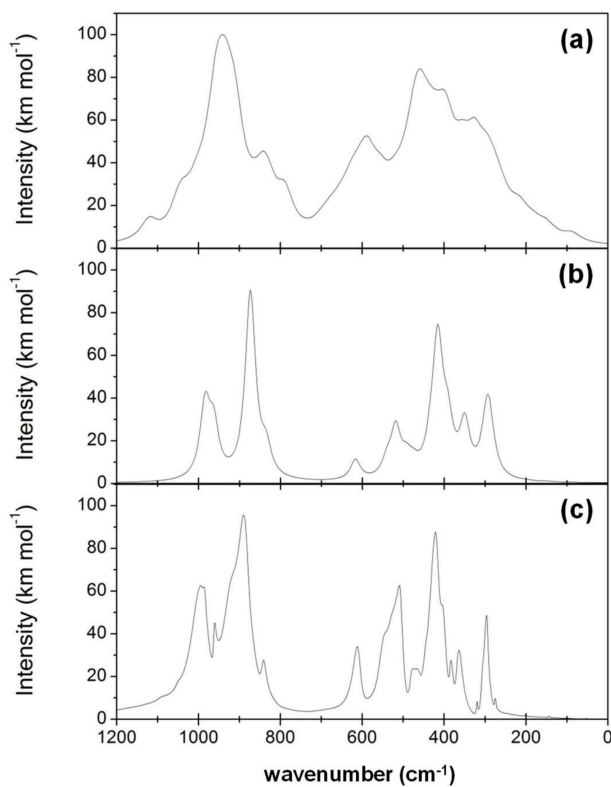


Figure 5. B3LYP-simulated IR spectra of the amorphous (a) and crystalline forsterite (b). The experimental spectrum of the crystalline forsterite is also included (c).

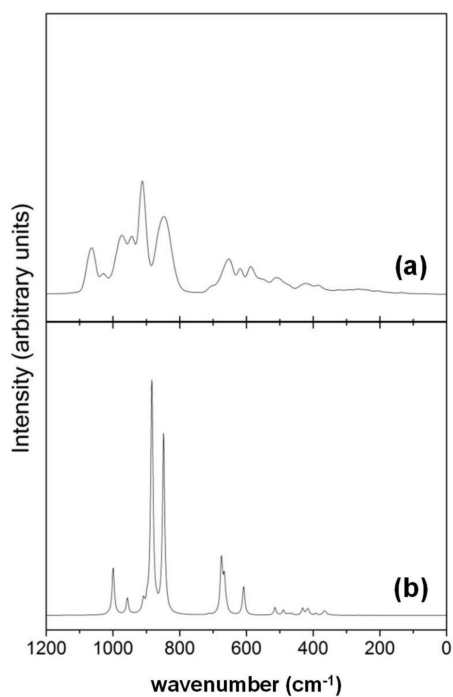


Figure 6. B3LYP-simulated Raman spectra of the amorphous (a) and crystalline forsterite (b).

Table 5. Active Raman frequencies (ν , in cm^{-1}) calculated in this work and their comparison with the experimental data. The shifts between the calculated and the experimental values ($\Delta\nu$) are also provided.

N	This Work		[121]		[119]		[60]		[59]		
	ν	I (%)	ν	$\Delta\nu$	ν	$\Delta\nu$	ν	$\Delta\nu$	ν	$\Delta\nu$	
A _g	1	212	0.05	184	28	183	29	183	29	183	29
	2	261	0.08	227	34	226	35	227	34	227	34
	3	351	0.11	304	47	304	47	305	46	305	46
	4	367	1.20	329	38	329	38	329	38	329	38
	5	391	0.78	339	52	332	59	340	51	340	51
	6	474	0.62	421	53	422	52	424	50	424	50
	7	608	12.4	544	64	545	63	546	62	545	63
	8	675	22.2	608	67	608	67	609	66	609	66
	9	848	81.1	824	24	824	24	826	22	826	22
	10	883	100	856	27	856	27	856	27	856	27
	11	999	20.6	966	33	965	34	966	33	966	33
B _{1g}	12	253	0.00	-	-	220	33	224	29	197	56
	13	294	0.06	-	-	274	20	260	34	265	29
	14	361	1.05	316	45	318	43	318	43	317	44
	15	417	1.68	-	-	351	66	-	-	-	-
	16	420	0.38	-	-	383	37	418	2	418	2
	17	489	2.21	434	55	434	55	434	55	434	55
	18	658	1.39	588	70	582	76	585	73	583	75
	19	713	0.43	-	-	632	81	632	81	632	81
	20	869	1.28	838	31	838	31	839	30	839	30
	21	897	3.37	866	31	866	31	866	31	866	31
	22	1012	0.37	-	-	975	37	976	36	976	36
B _{2g}	23	-	-	-	175	-	142	-	-	-	
	24	229	0.01	243	-14	242	-13	244	-15	244	-15
	25	343	0.17	-	-	323	20	324	19	324	19
	26	365	0.08	-	-	365	0	368	-3	365	0
	27	431	2.93	-	-	-	-	-	-	407	24
	28	463	0.69	434	29	439	24	441	22	438	25
	29	665	14.3	588	77	586	79	588	77	585	80
	30	956	6.98	882	74	881	75	884	72	881	75
B _{3g}	31	203	0.00	243	-40	-	-	226	-23	-	-
	32	296	0.00	-	-	286	10	272	24	-	-
	33	-	-	316	-	315	-	318	-	314	-
	34	369	0.31	373	-4	374	-5	376	-7	374	-5
	35	413	1.35	409	4	410	3	412	1	406	7
	36	-	-	-	-	435	-	-	-	466	-
	37	514	3.34	-	-	-	-	-	-	484	30
	38	670	2.82	588	82	592	78	595	75	591	79
	39	908	5.14	920	-12	920	-12	922	-14	920	-12

More interesting are the differences between the B3LYP-simulated crystalline and amorphous IR and Raman spectra. Crystal Fo presents a set of well-defined bands, in which the total active vibrations are not fully visualized in the form of bands because some are either overlapped with contiguous bands or present at very low intensities. The spectra of amorphous Fo are clearly different; that is, they are based on single broad bands. In particular, the IR and Raman spectra of amorphous Fo present three and two well-defined zones, respectively: for IR, one band between 1000–800 cm^{-1} , a peak at about 600 cm^{-1} , and another band between 500–300 cm^{-1} ; for Raman, bands between 1000–800 cm^{-1} and between 700–400 cm^{-1} . These regions correspond essentially to the Si–O stretching and O–Si–O bending vibrations, respectively. However, vibrations associated with rotations of the SiO₄ tetrahedra and translations of Mg²⁺ also contribute in the low region of the lower bands. The significant broadening and blending of the IR bands presented by amorphous Fo compared to the

crystal systems is due to the wider and more diverse distribution of bond lengths and angles given in the former system, which is typical in amorphous materials. In fact, the hyperfine structure of the IR spectra of amorphous Fo (built by bands consisting of single lines) presents a great number of active vibrational bands that, upon imposing band width, overlap each other, rendering squat-shaped bands. The presence of more active vibrational bands compared to the crystal system is mainly due to the lack of symmetry in amorphous Fo. This means that some vibrations that are inactive in the crystal system, according to selection rules, are active in the amorphous one. Moreover, the cell enlargement means that equivalent vibrations by the translational symmetry in the minimal unit cell are different in the super-cell, giving rise to the apparition of new vibrational bands. Astronomical IR and Raman measurements of cosmic silicates revealed that they are mainly in an amorphous state. The recorded spectra generally present two single broad bands at about 1000 cm^{-1} and 550 cm^{-1} , associated with the Si–O stretching and O–Si–O bending vibrations, respectively [28]. Our simulated vibrational results of the amorphous Fo are thus in line with the astronomical IR and Raman spectral features.

As anticipated in Computational Methods, the reflectance spectrum of a given 3D-periodic system can be simulated with the CRYSTAL code. An important ingredient for the construction of the reflectance curves is ϵ_{∞} , whose values are discussed above. The B3LYP-simulated reflectance spectra of Fo, both crystalline and amorphous, are shown in Figure 7. The reflectivity is separated according to the three crystallographic axes (a , b , and c), which for the crystal system, are coincident with the vibration symmetry (B_{3u} , B_{2u} , and B_{1u} , respectively). The topology of the simulated reflection curves of crystalline Fo perfectly matches with the experimental ones. A detailed analysis of the effect of different fitting procedures to properly reproduce the experimental reflectance spectra is provided in [88]. The B3LYP-simulated reflectance spectra of amorphous Fo is significantly different. The broad reflectance curves of the crystalline system are sharper and present more bands. This is, in line to what is mentioned above, due to the higher number of active vibrational modes in the amorphous systems.

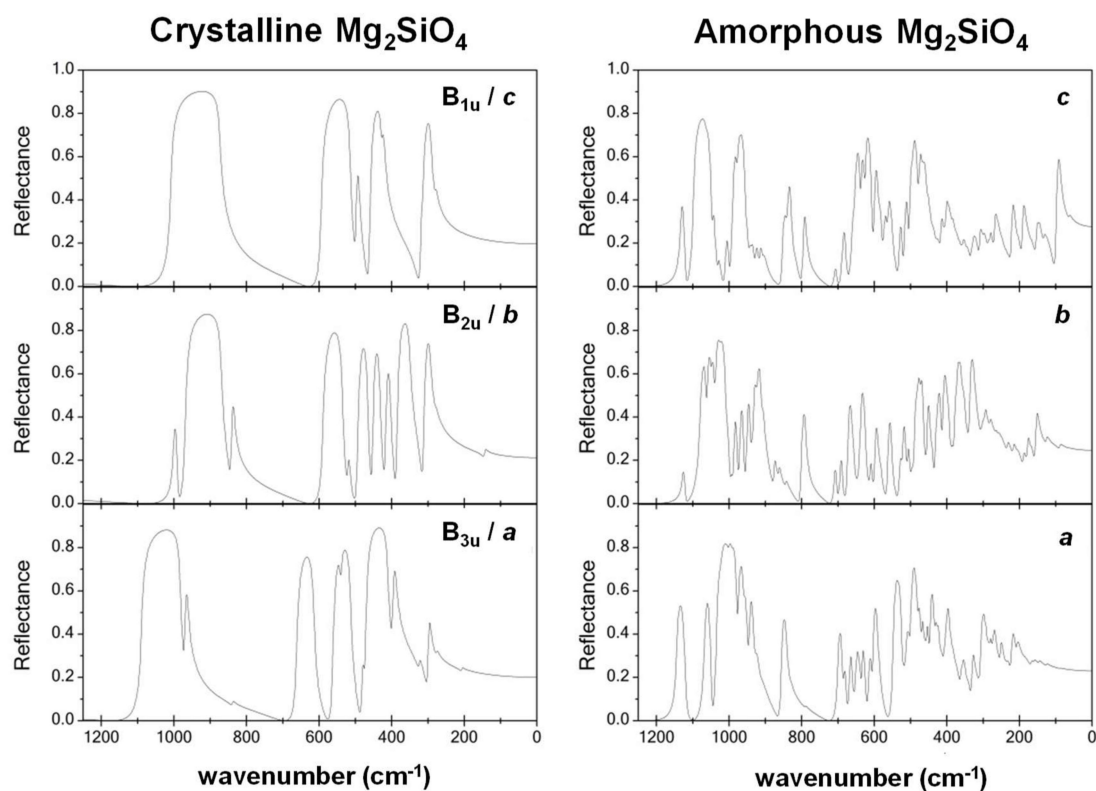


Figure 7. B3LYP-simulated reflectance spectra of the crystalline and amorphous forsterite along the a , b , and c directions.

3.2. Unit Cell Size Effects in the Amorphisation of the Mg_2SiO_4 System

In the previous section, a comprehensive comparison of the bulk physicochemical properties between crystalline and amorphous Mg_2SiO_4 is presented for a given unit cell. In this section, we aim to explore if the degree of amorphization is affected by the unit cell size. Our initial hypothesis is: the larger the unit cell, the more internal structural parameters to be randomly disordered, and accordingly, the larger the degree of amorphization. To demonstrate the validity (or not) of our hypothesis, different unit cell sizes have been considered, they have been amorphized, and an analysis of their structural, dielectric, and vibrational properties has been carried out by comparing these physicochemical properties between them. It is worth mentioning that the possible differences are associated with the different degree of amorphization, since, rigorously speaking, these physicochemical properties are not strictly size-dependent. However, we anticipate that the degree of amorphization is, in our systems, linked to the size of the unit cell and accordingly, these physicochemical properties are indeed ultimately related to the size of the unit cells.

To carry out these investigations, the following different super-cell sizes have been adopted: $1 \times 1 \times 2$, $2 \times 1 \times 2$, and $2 \times 2 \times 2$. The procedure to amorphize the corresponding crystalline systems was the same as that presented in the previous section; that is, classical MD simulations at 1800 K followed by B3LYP optimization of the resulting geometry to carry out the theoretical analysis. For all super-cell systems, the Mg–Mg and Mg–O $g(r)$ pair correlation functions are similar, showing several broad but distinguishable bands representing the different Mg–Mg and Mg–O shells (see Figure S3, Supplementary Materials). The similarity between the band widths of the different super-cell systems indicates that for all cases, the amorphization was definitely achieved.

The B3LYP-optimized structures of the different super-cell systems are shown in Figure 8, both in their atomistic and polyhedral forms. Table 6 presents the B3LYP-calculated lattice parameters, the range of the calculated Mg–O and Si–O bond lengths, and the volume and the density of the bulk materials. In Table 3, the mean values and the associated deviations of the internal O–Si–O and O–Mg–O angles compared to the ideal values are also reported for the $2 \times 1 \times 2$ and $2 \times 2 \times 2$ systems. By visual inspection of the images of Figure 8, one can identify that the larger the super-cell size, the more distorted the tetrahedral SiO_4 and octahedral MgO_6 building blocks. This larger distortion is also reflected by the mean values and the average deviations of the internal angles. In the $2 \times 1 \times 2$ and $2 \times 2 \times 2$ super-cell systems, they are larger than in the $1 \times 1 \times 2$ one. In addition to this, from a careful visual inspection of the atomistic structure of the amorphous systems, we realized that some unusual structural motifs are present in the $2 \times 1 \times 2$ and $2 \times 2 \times 2$ systems, which are absent in the $1 \times 1 \times 2$ one; in particular: (i) pentacoordinated Si atoms (SiO_5 adopting a trigonal pyramid-like geometry), (ii) pentacoordinated Mg atoms (MgO_5 adopting either square-pyramid-like or trigonal pyramid-like geometries), and (iii) tetraordinated Mg atoms (MgO_4 adopting highly distorted tetrahedral geometries). The presence of these structural motifs is indicative of the high degree of amorphization of these systems. In addition to this visual inspection, we also calculated the area under the $g(r)$ curves to measure the coordination numbers. For Si–O, they are 4.06, 4.12 ($2 \times 1 \times 2$), and 4.23 for the $1 \times 1 \times 2$, $2 \times 1 \times 2$, and $2 \times 2 \times 2$ systems, respectively, clearly indicating an increase of the Si–O coordination number for larger unit cells, due to the presence of these highly-coordinated motifs. It is worth mentioning that Si atoms with coordination numbers larger than 4 have been reported in a couple of synthesized minerals; namely, a high-pressure phase of $MgSi(OH)_6$ [126] and a dense phase (so-called phase D) of $MgSi(OH)_2O_4$ [127,128], predicted by means of theoretical calculations to occur in thaumasite [129], a naturally-occurring mineral present in the Earth's crust. For Mg–O, the coordination numbers are kept at 5.82 for all unit cell systems, probably due to compensation effects in the different Mg coordination spheres.

Table 6. B3LYP-optimized bond distance ranges and cell parameters of the $1 \times 1 \times 2$, $2 \times 1 \times 2$, and $2 \times 2 \times 2$ Mg_2SiO_4 bulk structures. Volumes and densities are also shown.

	$1 \times 1 \times 2$	$2 \times 1 \times 2$	$2 \times 2 \times 2$
Si–O (Å)	1.618–1.693	1.592–1.906	1.579–1.983
Mg–O (Å)	1.929–2.226	1.860–2.211	1.800–2.209
a (Å)	4.93	10.168	9.589
b (Å)	9.37	10.177	20.574
c (Å)	11.9	11.329	11.937
α (degrees)	87.4	89.6	85.7
β (degrees)	90.6	83.6	93.4
γ (degrees)	88.6	97.1	91.7
Volume (Å ³)	551.00	1156.77	2343.91
Density (g·cm ^{−3})	3.373	3.214	3.172

The calculated densities are reported in Table 7 and indicate that they decrease when the sizes of the super-cell increase; that is, $3.373 \text{ g}\cdot\text{cm}^{-3}$ ($1 \times 1 \times 2$) > $3.214 \text{ g}\cdot\text{cm}^{-3}$ ($2 \times 1 \times 2$) > $3.172 \text{ g}\cdot\text{cm}^{-3}$ ($2 \times 2 \times 2$). This is consistent with the fact that the larger the super-cell size, the larger the amorphous nature of the system. Indeed, by increasing the size of the super-cell, the structures can sport more defects and porosity, and consequently, the density is lower. The calculated ϵ_∞ constants along the x , y , and z directions (reported in Table 7) show the same pattern. An incremental increase of the super-cell size leads to a reduced dependency along the direction of the ϵ_∞ values as a consequence of the larger degree of disorder, which is equal along the three directions.

Table 7. Calculated high-frequency dielectric constants (ϵ_∞) for the B3LYP-optimized $1 \times 1 \times 2$, $2 \times 1 \times 2$, and $2 \times 2 \times 2$ Mg_2SiO_4 bulk structures along the x , y , and z directions.

	$1 \times 1 \times 2$	$2 \times 1 \times 2$	$2 \times 2 \times 2$
$\epsilon_{\infty,x}$	2.284	2.153	2.148
$\epsilon_{\infty,y}$	2.247	2.161	2.135
$\epsilon_{\infty,z}$	2.218	2.168	2.132

In relation to the vibrational properties, Figure 9 shows the simulated IR, Raman, and reflectance spectra. As mentioned above, the $1 \times 1 \times 2$ system presents three and two well-defined broad IR and Raman bands, respectively. In contrast, the IR spectrum of the $2 \times 2 \times 2$ system presents two largely broad bands; that is, the two bands in the low-frequency region of the $1 \times 1 \times 2$ system overlap in the $2 \times 2 \times 2$ system. Similar changes occur in the Raman spectrum: the two regions present in the $1 \times 1 \times 2$ system become fused in the $2 \times 2 \times 2$ system. The IR and Raman spectra of the $2 \times 1 \times 2$ system present intermediate profiles between those of the $1 \times 1 \times 2$ and the $2 \times 2 \times 2$ systems; that is, the different frequency regions clearly identified in the $1 \times 1 \times 2$ system are still identifiable, but are more diffuse. A similar transition in the topology of the reflectance spectra can be observed from the $1 \times 1 \times 2$ and $2 \times 1 \times 2$ to the $2 \times 2 \times 2$ systems. In this case, an increase of the unit cell size leads to spectra that present sharper and more bands due to the major number of independent active bands. All these changes in the topology of the vibrational-related spectra clearly indicate that there is a progressive increase of the amorphous nature from the $1 \times 1 \times 2$ to the $2 \times 2 \times 2$ super-cell systems.

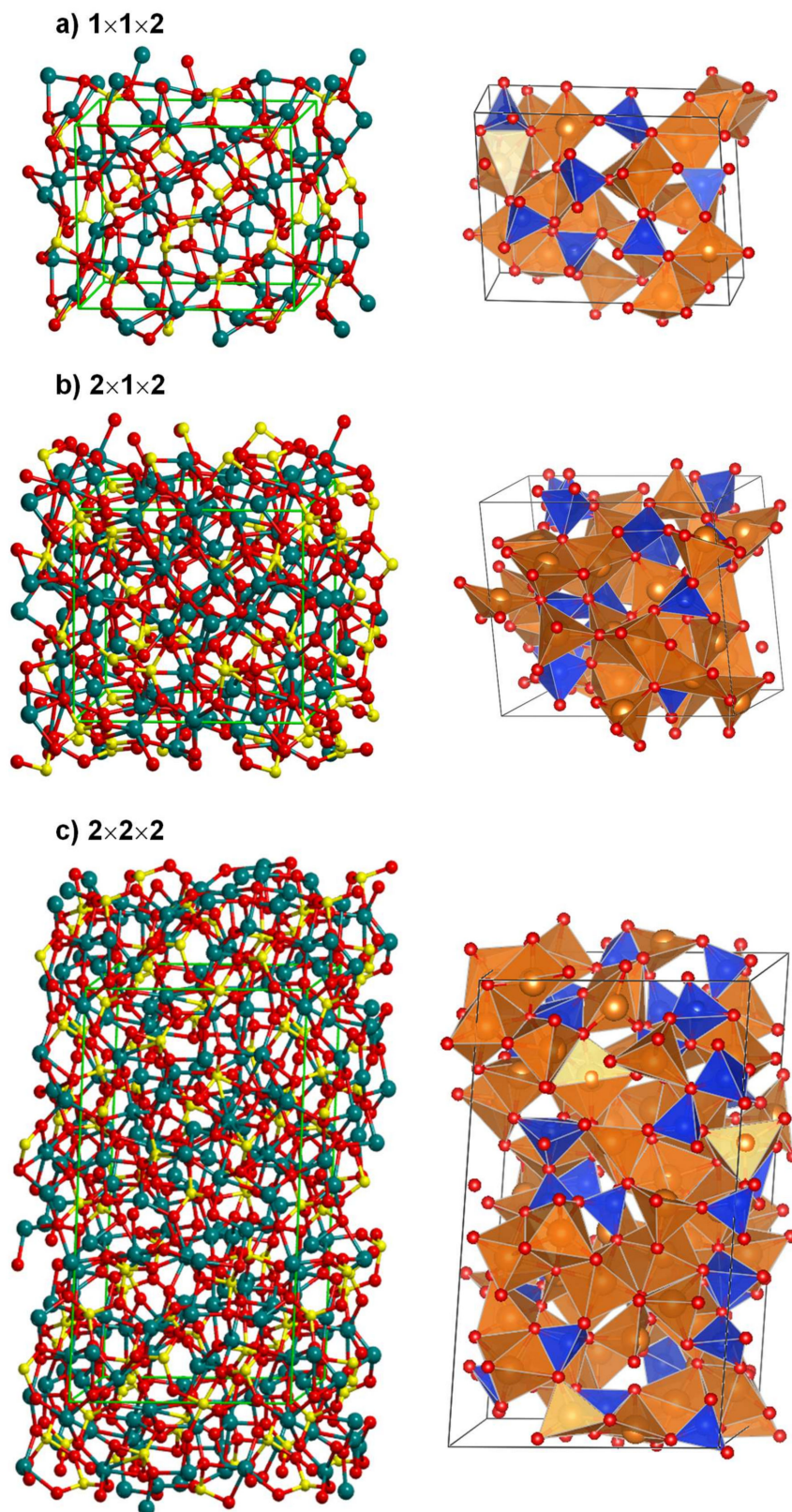


Figure 8. B3LYP-optimized structures of the bulk Mg_2SiO_4 adopting the $1 \times 1 \times 2$ (a), $2 \times 1 \times 2$ (b), and $2 \times 2 \times 2$ (c) super-cell configurations generated by classical MD simulations at $T = 1800$ K, both in the atomistic views (left) and in the polyhedral forms (right).

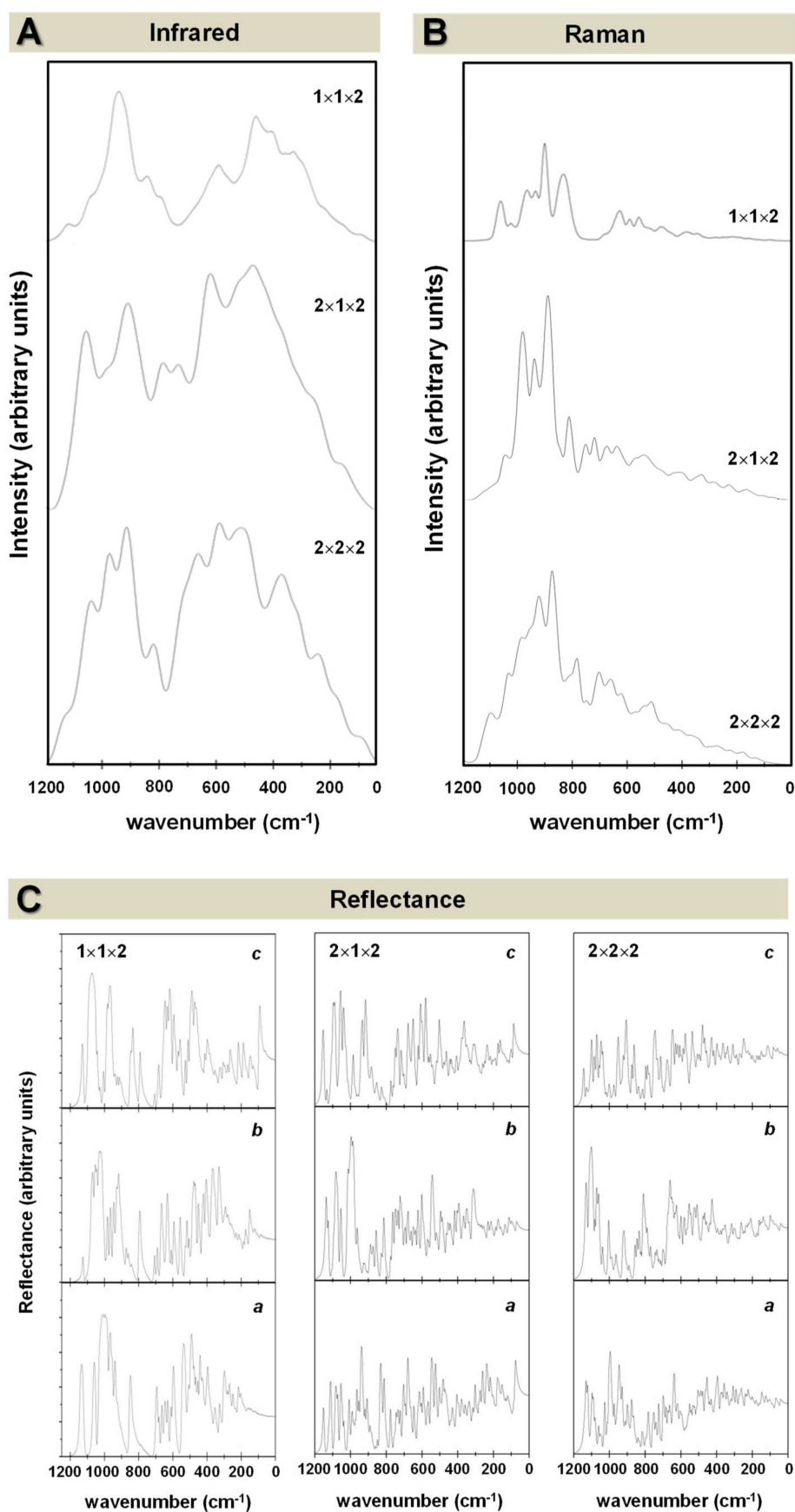


Figure 9. B3LYP-simulated infrared (A), Raman (B), and reflectance spectra along the *a*, *b*, and *c* directions (C) of the Mg₂SiO₄ bulk structures adopting the 1 × 1 × 2, 2 × 1 × 2, and 2 × 2 × 2 super-cell configurations.

4. Conclusions

By combining classical MD simulations with periodic DFT calculations, a detailed theoretical study on the structural, dielectric, and vibrational properties of Mg_2SiO_4 as a silicate test case has been presented. The amorphous structures for Mg_2SiO_4 have been generated using classical MD simulations at different temperatures within a melt-and-quench scheme, taking the crystalline phase as the initial guess structure. Periodic B3LYP calculations have been carried out to optimize the geometries of the generated structure and calculate their high-frequency dielectric constants and simulate the IR, Raman, and reflectance spectra. The most interesting points emerging from this work are:

- The combined approach of classical MD for structure evolution and quantum chemical DFT for electronic structure analysis is a reliable technique to investigate the physicochemical properties of silicates.
- The Mg–Mg and Mg–O pair correlation functions, $g(r)$, derived from the classical MD simulations indicate that an increase of the temperature produces broader profiles of $g(r)$, indicating a progressive loss of crystallinity with temperature.
- B3LYP-optimized geometries of the amorphous bulk systems present larger distributions of bond lengths and angles than the crystal analogues (for instance, the Si–O distance ranges, 1.618–1.693 Å vs 1.628–1.673 Å) due to the significant disorganization of the internal atomic positions. Consequently, the tetrahedral SiO_4 and octahedral MgO_6 motifs become largely distorted, which is characteristic of amorphous materials. Calculated densities of the amorphous bulks are lower than the crystalline ones; that is, 3.373 ($1 \times 1 \times 2$), 3.214 ($2 \times 1 \times 2$), 3.172 ($2 \times 2 \times 2$) versus 3.34 (crystalline), due to the presence of internal cavities produced during the amorphization process.
- Related to the high-frequency dielectric constants along the x , y , and z directions ($\epsilon_{\infty,x}$, $\epsilon_{\infty,y}$, and $\epsilon_{\infty,z}$), while in the crystalline Mg_2SiO_4 they are clearly different (2.571, 2.424, and 2.475, respectively), in agreement with the direction dependency caused by the inherently crystallinity of the system, in the amorphous phases, they are more similar (e.g., for the $2 \times 2 \times 2$ system, 2.148, 2.135, and 2.132, respectively), showing a convergence between the calculated $\epsilon_{\infty,x}$, $\epsilon_{\infty,y}$, and $\epsilon_{\infty,z}$ values. Accordingly, ϵ_{∞} values do not depend on a particular direction because the system is likewise disordered in all the directions.
- While the IR and Raman spectra of the crystalline phase present well-defined narrow bands covering the 1000–200 cm^{-1} region, the spectra of the amorphous analogues, due to the wider and more diverse distribution of lengths and angles, are dominated by broader bands caused by multiple bands overlapping; namely, for IR, three broad bands are observed (between 1000–800 cm^{-1} , a peak at 600 cm^{-1} , and between 500–300 cm^{-1}), while for Raman, two broad bands are observed (between 1000–800 cm^{-1} and between 700–400 cm^{-1}). The simulated spectra agree fairly well with those recorded for Mg_2SiO_4 in astrophysical environments, with the IR broad bands being centered at 1000 cm^{-1} and 500 cm^{-1} . In the case of reflectance spectra, the broad reflectance curves of the crystalline system change with bands increasing in sharpness and number for the amorphous systems, due to the presence of more active modes.
- Regarding the unit cell size effects, results clearly provide evidence that an increase of the unit cell size infers a larger degree of amorphization due to the presence of more internal degrees of freedom to be disordered.

The presented results can be useful in several aspects. From a computational point of view, from these amorphous bulk systems, one can generate slab surface models in the same amorphous state to carry out surface chemical studies (for instance, to study a given heterogeneous catalytic process). Additionally, results can be used as a benchmark for the development of force fields devoted to simulating amorphous/glassy silicates. The characterized spectroscopic properties can be stored in current astronomical databases and archives devoted to measuring spectroscopic properties of astrophysical silicate-based dust particles, to be compared with forthcoming results. Finally, they

can stimulate future experimental work in the synthesis and physicochemical characterization of amorphous forsterite under highly controllable conditions, whose results can be compared with the present ones.

Supplementary Materials: The following are available online at <http://www.mdpi.com/2075-163X/8/8/353/s1>, Figure S1: GULP-optimized structure for the bulk of the crystal Mg_2SiO_4 . View of the unit cell (left), view of the extended periodic system (right), Figure S2: Mg–Mg (a) and Mg–O (b) pair correlation functions derived from the MD simulations at the different temperatures accounting for periodic boundary conditions, Figure S3: Mg–Mg (a) and Mg–O (b) pair correlation functions derived from the classical MD simulations for the $1 \times 1 \times 2$, $2 \times 1 \times 2$ and $2 \times 2 \times 2$ systems, Table S1: Bond distance ranges (in Å) of the crystalline $1 \times 1 \times 1$ Mg_2SiO_4 bulk structures: experimental, GULP-optimized, and B3LYP and B3LYP-D2 optimized values, Table S2: Bond distance ranges (in Å) and lattice parameters (distances in Å, angles in degrees) of the amorphous $1 \times 1 \times 2$ Mg_2SiO_4 bulk structure optimized at B3LYP and B3LYP-D2 theory level, Scheme S1: Cell parameters and fractionary coordinates of the optimized systems.

Author Contributions: Conceptualization, A.R.; Methodology, Software, Validation, Formal Analysis, Investigation, Resources, and Data Curation, J.Á.M.-G. and J.N.-R; Writing—Original Draft Preparation, Writing—Review & Editing, and Visualization, J.Á.M.-G. and A.R.; Supervision, Project Administration and Funding Acquisition, A.R.

Funding: This research was funded by MINECO (Projects CTQ2014-60119-P and CTQ2017-89132-P) and DIUE (Projects 2014SGR482 and 2017SGR1320).

Acknowledgments: A.R. is indebted to “Ramón y Cajal” program. J.Á.M.-G. is indebted to “Europa Excelencia” program, supported by CTQ2013-40347-ERC.

Conflicts of Interest: The authors declare no conflict of interest. The funders had no role in the design of the study; in the collection, analyses, or interpretation of data; in the writing of the manuscript; and in the decision to publish the results.

References

1. Rimola, A.; Costa, D.; Sodupe, M.; Lambert, J.-F.; Ugliengo, P. Silica surface features and their role in the adsorption of biomolecules: Computational modeling and experiments. *Chem. Rev.* **2013**, *113*, 4216–4313. [[CrossRef](#)] [[PubMed](#)]
2. Fenoglio, I.; Prandi, L.; Tomatis, M.; Fubini, B. Free radical generation in the toxicity of inhaled mineral particles: The role of iron speciation at the surface of asbestos and silica. *Redox Rep.* **2001**, *6*, 235–241. [[CrossRef](#)] [[PubMed](#)]
3. Fubini, B.; Otero Areán, C. Chemical aspects of the toxicity of inhaled mineral dusts. *Chem. Soc. Rev.* **1999**, *28*, 373–381. [[CrossRef](#)]
4. Otero Areán, C.; Barceló, F.; Fenoglio, I.; Fubini, B.; Llabrés i Xamena, F.X.; Tomatis, M. Free radical activity of natural and heat treated amphibole asbestos. *J. Inorg. Chem.* **2001**, *83*, 211–216. [[CrossRef](#)]
5. Turci, F.; Colonna, M.; Tomatis, M.; Mantegna, S.; Cravotto, G.; Gulino, G.; Aldieri, E.; Ghigo, D.; Fubini, B. Surface reactivity and cell responses to chrysotile asbestos nanofibers. *Chem. Res. Toxicol.* **2012**, *25*, 884–894. [[CrossRef](#)] [[PubMed](#)]
6. Merget, R.; Bauer, T.; Küpper, H.; Philippou, S.; Bauer, H.; Breitstadt, R.; Bruening, T. Health hazards due to the inhalation of amorphous silica. *Arch. Toxicol.* **2002**, *75*, 625–634. [[CrossRef](#)] [[PubMed](#)]
7. Hench, L.L.; Polak, J.M. Third-generation biomedical materials. *Science* **2002**, *295*, 1014–1017. [[CrossRef](#)] [[PubMed](#)]
8. Vallet-Regí, M.; Balas, F.; Arcos, D. Mesoporous materials for drug delivery. *Angew. Chem. Int. Edit.* **2007**, *46*, 7548–7558. [[CrossRef](#)] [[PubMed](#)]
9. Ceresoli, D.; Vanderbilt, D. Structural and dielectric properties of amorphous ZrO_2 and HfO_2 . *Phys. Rev. B* **2006**, *74*, 125108. [[CrossRef](#)]
10. Wang, Y.; Zahid, F.; Wang, J.; Guo, H. Structure and dielectric properties of amorphous high-k oxides: HfO_2 , ZrO_2 , and their alloys. *Phys. Rev. B* **2012**, *85*, 224110. [[CrossRef](#)]
11. Zhao, X.; Ceresoli, D.; Vanderbilt, D. Structural, electronic, and dielectric properties of amorphous ZrO_2 from *ab initio* molecular dynamics. *Phys. Rev. B* **2005**, *71*, 085107. [[CrossRef](#)]
12. Hofmeister, A.M. Single-crystal absorption and reflection infrared spectroscopy of forsterite and fayalite. *Phys. Chem. Miner.* **1987**, *14*, 499–513. [[CrossRef](#)]

13. Madon, M.; Price, G.D. Infrared spectroscopy of the polymorphic series (enstatite, ilmenite, and perovskite) of MgSiO_3 , MgGeO_3 , and MnGeO_3 . *J. Geophys. Res. Solid Earth* **1989**, *94*, 15687–15701. [[CrossRef](#)]
14. Fabian, D.; Jäger, C.; Henning, T.; Dorschner, J.; Mutschke, H. Steps toward interstellar silicate mineralogy V. Thermal evolution of amorphous magnesium silicates and silica. *Astron. Astrophys.* **2000**, *364*, 282–292.
15. Henning, T.; Mutschke, H. Low-temperature infrared properties of cosmic dust analogues. *Astron. Astrophys.* **1997**, *327*, 743–754.
16. Jäger, C.; Molster, F.J.; Dorschner, J.; Henning, T.; Mutschke, H.; Waters, L.B.F.M. Steps toward interstellar silicate mineralogy. IV. The crystalline revolution. *Astron. Astrophys.* **1998**, *339*, 904–916.
17. Billinge, S.J.L.; Levin, I. The problem with determining atomic structure at the nanoscale. *Science* **2007**, *316*, 561–565. [[CrossRef](#)] [[PubMed](#)]
18. Tilocca, A. Current challenges in atomistic simulations of glasses for biomedical applications. *Phys. Chem. Chem. Phys.* **2014**, *16*, 3874–3880. [[CrossRef](#)] [[PubMed](#)]
19. Berardo, E.; Pedone, A.; Ugliengo, P.; Corno, M. DFT Modeling of 45S5 and 77S soda-lime phospho-silicate glass surfaces: Clues on different bioactivity mechanism. *Langmuir* **2013**, *29*, 5749–5759. [[CrossRef](#)] [[PubMed](#)]
20. Bondi, R.J.; Lee, S.; Hwang, G.S. First-principles study of the mechanical and optical properties of amorphous hydrogenated silicon and silicon-rich silicon oxide. *Phys. Rev. B* **2010**, *81*, 195207. [[CrossRef](#)]
21. Corno, M.; Pedone, A.; Dovesi, R.; Ugliengo, P. B3LYP simulation of the full vibrational spectrum of 45S5 bioactive silicate glass compared to v-silica. *Chem. Mater.* **2008**, *20*, 5610–5621. [[CrossRef](#)]
22. Karazhanov, S.Z.; Kroll, P.; Holt, A.; Bentzen, A.; Ulyashin, A. Comparative analysis of electronic structure and optical properties of crystalline and amorphous silicon nitrides. *J. Appl. Phys.* **2009**, *106*, 053717. [[CrossRef](#)]
23. Kroll, P. A DFT study of amorphous silicon oxynitride. *J. Non-Cryst. Solids* **2005**, *351*, 1127–1132. [[CrossRef](#)]
24. Landmann, M.; Köhler, T.; Rauls, E.; Frauenheim, T.; Schmidt, W.G. The atomic structure of ternary amorphous $\text{Ti}_x\text{Si}_{1-x}\text{O}_2$ hybrid oxides. *J. Phys. Condens. Matter* **2014**, *26*, 253201. [[CrossRef](#)] [[PubMed](#)]
25. Lee, S.; Bondi, R.J.; Hwang, G.S. *Ab initio* parameterized valence force field for the structure and energetics of amorphous SiO_x ($0 < x < 2$) materials. *Phys. Rev. B* **2011**, *84*, 045202.
26. Umari, P.; Pasquarello, A. Infrared and raman spectra of disordered materials from first principles. *Diam. Relat. Mater.* **2005**, *14*, 1255–1261. [[CrossRef](#)]
27. Marquardt, K.; Faul, U.H. The structure and composition of olivine grain boundaries: 40 years of studies, status and current developments. *Phys. Chem. Miner.* **2018**, *45*, 139–172. [[CrossRef](#)]
28. Henning, T. Cosmic silicates. *Annu. Rev. Astron. Astrophys.* **2010**, *48*, 21–46. [[CrossRef](#)]
29. Mumma, M.J.; Charnley, S.B. The chemical composition of comets—Emerging taxonomies and natal heritage. *Annu. Rev. Astron. Astrophys.* **2011**, *49*, 471–524. [[CrossRef](#)]
30. Rubin, A.E. Mineralogy of meteorite groups. *Meteorit. Planet. Sci.* **1997**, *32*, 231–247. [[CrossRef](#)]
31. Molster, F.; Kemper, C. Crystalline silicates. *Space Sci. Rev.* **2005**, *119*, 3–28. [[CrossRef](#)]
32. Vidali, G. H_2 Formation on interstellar grains. *Chem. Rev.* **2013**, *113*, 8762–8782. [[CrossRef](#)] [[PubMed](#)]
33. Hama, T.; Watanabe, N. Surface processes on interstellar amorphous solid water: Adsorption, diffusion, tunneling reactions, and nuclear-spin conversion. *Chem. Rev.* **2013**, *113*, 8783–8839. [[CrossRef](#)] [[PubMed](#)]
34. Van Dishoeck, E.F.; Herbst, E.; Neufeld, D.A. Interstellar water chemistry: From laboratory to observations. *Chem. Rev.* **2013**, *113*, 9043–9085. [[CrossRef](#)] [[PubMed](#)]
35. Shankland, T.J.; Hemmenway, K. Synthesis of forsterite crystals. *Am. Mineral.* **1963**, *48*, 200.
36. Brindley, G.W.; Hayami, R. Kinetics and mechanism of formation of forsterite (Mg_2SiO_4) by solid state reaction of MgO and SiO_2 . *Phil. Mag. Lett.* **1965**, *12*, 505–514. [[CrossRef](#)]
37. Shankland, T.J. Synthetic forsterite. *Ceram. Bull.* **1967**, *46*, 1160–1162.
38. Cunha-Duncan Flavia, N.; Bradt Richard, C. Synthesis of magnesium aluminate spinels from bauxites and magnesias. *J. Am. Ceram. Soc.* **2004**, *85*, 2995–3003. [[CrossRef](#)]
39. Kazakos, A.; Komarneni, S.; Roy, R. Preparation and densification of forsterite (Mg_2SiO_4) by nanocomposite sol-gel processing. *Mater. Lett.* **1990**, *9*, 405–409. [[CrossRef](#)]
40. Park, D.G.; Duchamp, J.C.; Duncan, T.M.; Burlitch, J.M. Preparation of forsterite by pyrolysis of a xerogel: The effect of water. *Chem. Mater.* **1994**, *6*, 1990–1995. [[CrossRef](#)]
41. Ban, T.; Ohya, Y.; Takahashi, Y. Low-temperature crystallization of forsterite and orthoenstatite. *J. Am. Ceram. Soc.* **2004**, *82*, 22–26. [[CrossRef](#)]

42. Finch, C.B.; Clark, G.W. Czochralski growth of single-crystal Mg_2SiO_4 (forsterite). *J. Cryst. Growth* **1971**, *8*, 307–308. [[CrossRef](#)]
43. Takei, H.; Hosoya, S.; Ozima, M. Synthesis of large single crystals of silicates and titanates. In *Materials Science of the Earth's Interior*; Sunagawa, I., Ed.; Terra Scientific Publishing: Tokyo, Japan, 1984; pp. 107–130.
44. Ito, K.; Sato, H.; Takei, H.; Tamada, O.; Kitazawa, T. Synthesis of large high-quality forsterite single crystals to 200 mm length and its significance. *Geochem. Geophys. Geosyst.* **2003**, *4*. [[CrossRef](#)]
45. Williams, Q.; McMillan, P.; Cooney, T.F. Vibrational spectra of olivine composition glasses: The Mg-Mn join. *Phys. Chem. Miner.* **1989**, *16*, 352–359. [[CrossRef](#)]
46. Cooney, T.F.; Sharma, S.K. Structure of glasses in the systems Mg_2SiO_4 - Fe_2SiO_4 , Mn_2SiO_4 - Fe_2SiO_4 , Mg_2SiO_4 - $CaMgSiO_4$, and Mn_2SiO_4 - $CaMnSiO_4$. *J. Non-Cryst. Solids* **1990**, *122*, 10–32. [[CrossRef](#)]
47. Tangeman, J.A.; Phillips, B.L.; Navrotsky, A.; Weber, J.K.R.; Hixson, A.D.; Key, T.S. Vitreous forsterite (Mg_2SiO_4): Synthesis, structure, and thermochemistry. *Geophys. Res. Lett.* **2001**, *28*, 2517–2520. [[CrossRef](#)]
48. Thompson, S.P.; Evans, A.; Jones, A.P. Structural evolution in thermally processed silicates. *Astron. Astrophys.* **1996**, *308*, 309–320.
49. Hanada, T.; Soga, N.; Tachibana, T. Coordination state of magnesium ions in rf-sputtered amorphous films in the system MgO-SiO₂. *J. Non-Cryst. Solids* **1988**, *105*, 39–44. [[CrossRef](#)]
50. Jeanloz, R.; Ahrens, T.J.; Lally, J.S.; Nord, G.L.; Christie, J.M.; Heuer, A.H. Shock-produced olivine glass: First observation. *Science* **1977**, *197*, 457. [[CrossRef](#)] [[PubMed](#)]
51. Kosanović, C.; Stubičar, N.; Tomašić, N.; Bermanec, V.; Stubičar, M. Synthesis of a forsterite powder by combined ball milling and thermal treatment. *J. Alloys Compd.* **2005**, *389*, 306–309. [[CrossRef](#)]
52. Mirhadi, S.M.; Forghani, A.; Tavangarian, F. A modified method to synthesize single-phase forsterite nanoparticles at low temperature. *Ceram. Int.* **2016**, *42*, 7974–7979. [[CrossRef](#)]
53. Mennella, V.; Brucato, J.R.; Colangeli, L. Carbon and silicate grains in the laboratory as analogues of cosmic dust. *Spectrochim. Acta Part A* **2001**, *57*, 787–795. [[CrossRef](#)]
54. Colangeli, L.; Henning, T.; Brucato, J.R.; Clément, D.; Fabian, D.; Guillois, O.; Huisken, F.; Jäger, C.; Jessberger, E.K.; Jones, A.; et al. The role of laboratory experiments in the characterisation of silicon-based cosmic material. *Astron. Astrophys. Rev.* **2003**, *11*, 97–152. [[CrossRef](#)]
55. Brunetto, R.; Roush, T.L.; Marra, A.C.; Orofino, V. Optical characterization of laser ablated silicates. *Icarus* **2007**, *191*, 381–393. [[CrossRef](#)]
56. Tavangarian, F.; Emadi, R. Synthesis of nanocrystalline forsterite (Mg_2SiO_4) powder by combined mechanical activation and thermal treatment. *Mater. Res. Bull.* **2010**, *45*, 388–391. [[CrossRef](#)]
57. Tavangarian, F.; Emadi, R. Mechanochemical synthesis of single phase nanocrystalline forsterite powder. *Int. J. Mod. Phys. B* **2010**, *24*, 343–350. [[CrossRef](#)]
58. Nurbaiti, U.; Zainuri, T.M.; Pratapa, S. Synthesis of microforsterite using derived-amorphous-silica of silica sands. *AIP Conf. Proc.* **2016**, *1725*, 020056.
59. Servoin, J.L.; Piriou, B. Infrared reflectivity and raman scattering of Mg_2SiO_4 single crystal. *Phys. Status Solidi B* **1973**, *55*, 677–686. [[CrossRef](#)]
60. Iishi, K. Lattice dynamics of forsterite. *Am. Mineral.* **1978**, *63*, 1198–1208.
61. Gervais, F.; Blin, A.; Massiot, D.; Coutures, J.P.; Chopinet, M.H.; Naudin, F. Infrared reflectivity spectroscopy of silicate glasses. *J. Non-Cryst. Solids* **1987**, *89*, 384–401. [[CrossRef](#)]
62. Brucato, J.R.; Colangeli, L.; Mennella, V.; Palumbo, P.; Bussoletti, E. Mid-infrared spectral evolution of thermally annealed amorphous pyroxene. *Astron. Astrophys.* **1999**, *348*, 1012–1019.
63. Abdi Maghsoudlou, M.S.; Ebadzadeh, T.; Sharafi, Z.; Arabi, M.; Zahabi, K.R. Synthesis and sintering of nano-sized forsterite prepared by short mechanochemical activation process. *J. Alloys Compd.* **2016**, *678*, 290–296. [[CrossRef](#)]
64. Suzuki, N.; Kimura, S.; Nakada, T.; Kaito, C.; Saito, Y.; Koike, C. Correlation between crystallographic structure and infrared spectra of silicon oxide films containing iron or magnesium atoms. *Meteorit. Planet. Sci.* **2010**, *35*, 1269–1273. [[CrossRef](#)]
65. Tsuchiyama, A. Condensation experiments using a forsterite evaporation source in H₂ at low pressures. *Mineral. J.* **1998**, *20*, 59–80. [[CrossRef](#)]
66. Black, J.R.; Carroll, S.A.; Haese, R.R. Rates of mineral dissolution under CO₂ storage conditions. *Chem. Geol.* **2015**, *399*, 134–144. [[CrossRef](#)]

67. Meysman, F.J.R.; Montserrat, F. Negative CO₂ emissions via enhanced silicate weathering in coastal environments. *Biol. Lett.* **2017**, *13*, 20160905. [[CrossRef](#)] [[PubMed](#)]
68. Montserrat, F.; Renforth, P.; Hartmann, J.; Leermakers, M.; Knops, P.; Meysman, F.J.R. Olivine dissolution in seawater: Implications for CO₂ sequestration through enhanced weathering in coastal environments. *Environ. Sci. Technol.* **2017**, *51*, 3960–3972. [[CrossRef](#)] [[PubMed](#)]
69. Quadery, A.H.; Pacheco, S.; Au, A.; Rizzacasa, N.; Nichols, J.; Le, T.; Glasscock, C.; Schelling, P.K. Atomic-scale simulation of space weathering in olivine and orthopyroxene. *J. Geophys. Res. Planets* **2015**, *120*, 643–661. [[CrossRef](#)]
70. Strefler, J.; Amann, T.; Bauer, N.; Kriegler, E.; Hartmann, J. Potential and costs of carbon dioxide removal by enhanced weathering of rocks. *Environ. Res. Lett.* **2018**, *13*. [[CrossRef](#)]
71. Ramesh, S.; Yaghoubi, A.; Sara Lee, K.Y.; Christopher Chin, K.M.; Purbolaksono, J.; Hamdi, M.; Hassan, M.A. Nanocrystalline forsterite for biomedical applications: Synthesis, microstructure and mechanical properties. *J. Mech. Behav. Biomed. Mater.* **2013**, *25*, 63–69. [[CrossRef](#)] [[PubMed](#)]
72. Samadikuchaksaraei, A.; Gholipourmalekabadi, M.; Farhadhosseinabadi, B.; Rezvani, Z.; Mozafari, M. Carboxymethyl chitosan/forsterite bone tissue engineering scaffolds: Correlations between composition and physico-chemical characteristics. *Biointerf. Res. Appl. Chem.* **2016**, *6*, 1222–1228.
73. Kharaziha, M.; Fathi, M.H.; Edris, H. Development of novel aligned nanofibrous composite membranes for guided bone regeneration. *J. Mech. Behav. Biomed. Mater.* **2013**, *24*, 9–20. [[CrossRef](#)] [[PubMed](#)]
74. Yazdanpanah, A.; Kamalian, R.; Moztarzadeh, F.; Mozafari, M.; Ravarian, R.; Tayebi, L. Enhancement of fracture toughness in bioactive glass-based nanocomposites with nanocrystalline forsterite as advanced biomaterials for bone tissue engineering applications. *Ceram. Int.* **2012**, *38*, 5007–5014. [[CrossRef](#)]
75. Diba, M.; Fathi, M.H.; Kharaziha, M. Novel forsterite/polycaprolactone nanocomposite scaffold for tissue engineering applications. *Mater. Lett.* **2011**, *65*, 1931–1934. [[CrossRef](#)]
76. Yang, H.M.; Shi, J.X.; Gong, M.L.; Cheah, K.W. Synthesis and photo luminescence of Eu³⁺- or Tb³⁺-doped Mg₂SiO₄ nanoparticles prepared by a combined novel approach. *J. Lumin.* **2006**, *118*, 257–264. [[CrossRef](#)]
77. Naik, R.; Prashantha, S.C.; Nagabhushana, H.; Sharma, S.C.; Nagabhushana, B.M.; Nagaswarupa, H.P.; Premkumar, H.B. Low temperature synthesis and photoluminescence properties of red emitting Mg₂SiO₄:Eu³⁺ nanophosphor for near UV light emitting diodes. *Sens. Actuators B* **2014**, *195*, 140–149. [[CrossRef](#)]
78. Zampiva, R.Y.S.; Acauan, L.H.; Venturini, J.; Garcia, J.A.M.; da Silva, D.S.; Han, Z.H.; Kassab, L.R.P.; Wetter, N.U.; Agarwal, A.; Alves, A.K.; et al. Tunable green/red luminescence by infrared upconversion in biocompatible forsterite nanoparticles with high erbium doping uptake. *Opt. Mater.* **2018**, *76*, 407–415. [[CrossRef](#)]
79. Dovesi, R.; Orlando, R.; Erba, A.; Zicovich-Wilson, C.M.; Civalieri, B.; Casassa, S.; Maschio, L.; Ferrabone, M.; De La Pierre, M.; D’Arco, P.; et al. CRYSTAL14: A program for the ab initio investigation of crystalline solids. *Int. J. Quantum Chem.* **2014**, *114*, 1287–1317. [[CrossRef](#)]
80. Born, M.; Huang, K. *Dynamical Theory of Crystal Lattices*; Oxford University Press: Oxford, UK, 1954; 420p.
81. Gale, J.D.; Rohl, A.L. The general utility lattice program (GULP). *Mol. Simul.* **2003**, *29*, 291–341. [[CrossRef](#)]
82. Flikkema, E.; Bromley, S.T. A new interatomic potential for nanoscale silica. *Chem. Phys. Lett.* **2003**, *378*, 622–629. [[CrossRef](#)]
83. Hassanali, A.A.; Singer, S.J. Model for the water—Amorphous silica interface: The undissociated surface. *J. Phys. Chem. B* **2007**, *111*, 11181–11193. [[CrossRef](#)] [[PubMed](#)]
84. Roberts, C.; Johnston, R.L. Investigation of the structures of MgO clusters using a genetic algorithm. *Phys. Chem. Chem. Phys.* **2001**, *3*, 5024–5034. [[CrossRef](#)]
85. Becke, A.D. Density-functional thermochemistry. III. The role of exact exchange. *J. Chem. Phys.* **1993**, *98*, 5648–5652. [[CrossRef](#)]
86. Lee, C.; Yang, W.; Parr, R.G. Development of the colle-salvetti correlation-energy formula into a functional of the electron density. *Phys. Rev. B* **1988**, *37*, 785–789. [[CrossRef](#)]
87. Civalieri, B.; D’Arco, P.; Orlando, R.; Saunders, V.R.; Dovesi, R. Hartree–Fock geometry optimisation of periodic systems with the CRYSTAL code. *Chem. Phys. Lett.* **2001**, *348*, 131–138. [[CrossRef](#)]
88. De La Pierre, M.; Carteret, C.; Orlando, R.; Dovesi, R. Use of *Ab initio* methods for the interpretation of the experimental IR reflectance spectra of crystalline compounds. *J. Comput. Chem.* **2013**, *34*, 1476–1485. [[CrossRef](#)] [[PubMed](#)]

89. De La Pierre, M.; Orlando, R.; Maschio, L.; Doll, K.; Ugliengo, P.; Dovesi, R. Performance of six functionals (LDA, PBE, PBESOL, B3LYP, PBE0, and WC1LYP) in the simulation of vibrational and dielectric properties of crystalline compounds. The case of forsterite Mg_2SiO_4 . *J. Comput. Chem.* **2011**, *32*, 1775–1784. [[CrossRef](#)] [[PubMed](#)]
90. Noel, Y.; Catti, M.; D'Arco, P.; Dovesi, R. The vibrational frequencies of forsterite Mg_2SiO_4 : An all-electron *ab initio* study with the CRYSTAL code. *Phys. Chem. Miner.* **2006**, *33*, 383–393. [[CrossRef](#)]
91. Noel, Y.; De La Pierre, M.; Maschio, L.; Rérat, M.; Zicovich-Wilson, C.M.; Dovesi, R. Electronic structure, dielectric properties and infrared vibrational spectrum of fayalite: An *ab initio* simulation with an all-electron gaussian basis set and the B3LYP functional. *Int. J. Quantum Chem.* **2012**, *112*, 2098–2108. [[CrossRef](#)]
92. Grimme, S. Semiempirical GGA-type density functional constructed with a long-range dispersion correction. *J. Comput. Chem.* **2006**, *27*, 1787–1799. [[CrossRef](#)] [[PubMed](#)]
93. Monkhorst, H.J.; Pack, J.D. Special points for brillouin-zone integrations. *Phys. Rev. B* **1976**, *13*, 5188–5192. [[CrossRef](#)]
94. Pascale, F.; Zicovich-Wilson, C.M.; López Gejo, F.; Civalleri, B.; Orlando, R.; Dovesi, R. The calculation of the vibrational frequencies of crystalline compounds and its implementation in the CRYSTAL code. *J. Comput. Chem.* **2004**, *25*, 888–897. [[CrossRef](#)] [[PubMed](#)]
95. Zicovich-Wilson, C.M.; Bert, A.; Roetti, C.; Dovesi, R.; Saunders, V.R. Characterization of the electronic structure of crystalline compounds through their localized wannier functions. *J. Chem. Phys.* **2002**, *116*, 1120–1127. [[CrossRef](#)]
96. Zicovich-Wilson, C.M.; Dovesi, R.; Saunders, V.R. A General method to obtain well localized wannier functions for composite energy bands in linear combination of atomic orbital periodic calculations. *J. Chem. Phys.* **2001**, *115*, 9708–9719. [[CrossRef](#)]
97. Zicovich-Wilson, C.M.; Torres, F.J.; Pascale, F.; Valenzano, L.; Orlando, R.; Dovesi, R. *Ab initio* simulation of the IR spectra of pyrope, grossular, and andradite. *J. Comput. Chem.* **2008**, *29*, 2268–2278. [[CrossRef](#)] [[PubMed](#)]
98. Ferrero, M.; Civalleri, B.; Rérat, M.; Orlando, R.; Dovesi, R. The calculation of the static first and second susceptibilities of crystalline urea: A comparison of Hartree-Fock and density functional theory results obtained with the periodic coupled perturbed Hartree-Fock/Kohn-Sham scheme. *J. Chem. Phys.* **2009**, *131*, 214704. [[CrossRef](#)] [[PubMed](#)]
99. Ferrero, M.; Rérat, M.; Orlando, R.; Dovesi, R. The calculation of static polarizabilities of 1-3D periodic compounds. The implementation in the crystal code. *J. Comput. Chem.* **2008**, *29*, 1450–1459. [[CrossRef](#)] [[PubMed](#)]
100. Carteret, C.; De La Pierre, M.; Dossot, M.; Pascale, F.; Erba, A.; Dovesi, R. The vibrational spectrum of CaCO_3 aragonite: A combined experimental and quantum-mechanical investigation. *J. Chem. Phys.* **2013**, *138*, 014201. [[CrossRef](#)] [[PubMed](#)]
101. De La Pierre, M.; Carteret, C.; Maschio, L.; André, E.; Orlando, R.; Dovesi, R. The raman spectrum of CaCO_3 polymorphs calcite and aragonite: A combined experimental and computational study. *J. Chem. Phys.* **2014**, *140*, 164509. [[CrossRef](#)] [[PubMed](#)]
102. Lacivita, V.; Erba, A.; Noël, Y.; Orlando, R.; D'Arco, P.; Dovesi, R. Zinc oxide nanotubes: An *ab initio* investigation of their structural, vibrational, elastic, and dielectric properties. *J. Chem. Phys.* **2013**, *138*, 214706. [[CrossRef](#)] [[PubMed](#)]
103. Maschio, L.; Demichelis, R.; Orlando, R.; Pierre, M.D.L.; Mahmoud, A.; Dovesi, R. The raman spectrum of grossular garnet: A quantum mechanical simulation of wavenumbers and intensities. *J. Raman Spectrosc.* **2014**, *45*, 710–715. [[CrossRef](#)]
104. Maschio, L.; Kirtman, B.; Salustro, S.; Zicovich-Wilson, C.M.; Orlando, R.; Dovesi, R. Raman spectrum of pyrope garnet. A quantum mechanical simulation of frequencies, intensities, and isotope shifts. *J. Phys. Chem. A* **2013**, *117*, 11464–11471. [[CrossRef](#)] [[PubMed](#)]
105. Maul, J.; Erba, A.; Santos, I.M.G.; Sambrano, J.R.; Dovesi, R. In silico infrared and raman spectroscopy under pressure: The case of CaSnO_3 perovskite. *J. Chem. Phys.* **2015**, *142*, 014505. [[CrossRef](#)] [[PubMed](#)]
106. Prencipe, M.; Maschio, L.; Kirtman, B.; Salustro, S.; Erba, A.; Dovesi, R. Raman spectrum of $\text{NaAlSi}_2\text{O}_6$ jadeite. A quantum mechanical simulation. *J. Raman Spectrosc.* **2014**, *45*, 703–709. [[CrossRef](#)]

107. Ricca, C.; Grishin, A.; Ringuede, A.; Cassir, M.; Adamo, C.; Labat, F. Modeling composite electrolytes for low-temperature solid oxide fuel cell application: Structural, vibrational and electronic features of carbonate-oxide interfaces. *J. Mater. Chem. A* **2016**, *4*, 17473–17482. [[CrossRef](#)]
108. Schneider, A.G.; Schomborg, L.; Ulpe, A.C.; Rüscher, C.H.; Bredow, T. Structure, vibrational spectra and ¹¹B-NMR chemical shift of Na₈[AlSiO₄]₆(B(OH)₄)₂: Comparison of theory and experiment. *J. Phys. Chem. A* **2016**, *120*, 7503–7509. [[CrossRef](#)] [[PubMed](#)]
109. Zicovich-Wilson, C.M.; Pascale, F.; Roetti, C.; Saunders, V.R.; Orlando, R.; Dovesi, R. Calculation of the vibration frequencies of α-Quartz: The effect of hamiltonian and basis set. *J. Comput. Chem.* **2004**, *25*, 1873–1881. [[CrossRef](#)] [[PubMed](#)]
110. Ferrero, M.; Rérat, M.; Kirtman, B.; Dovesi, R. Calculation of first and second static hyperpolarizabilities of one- to three-dimensional periodic compounds. Implementation in the CRYSTAL code. *J. Chem. Phys.* **2008**, *129*, 244110. [[CrossRef](#)] [[PubMed](#)]
111. Ferrero, M.; Rérat, M.; Orlando, R.; Dovesi, R. Coupled perturbed hartree-fock for periodic systems: The role of symmetry and related computational aspects. *J. Chem. Phys.* **2008**, *128*, 014110. [[CrossRef](#)] [[PubMed](#)]
112. Baranek, P.; Zicovich-Wilson, C.M.; Roetti, C.; Orlando, R.; Dovesi, R. Well localized crystalline orbitals obtained from bloch functions: The case of KNbO₃. *Phys. Rev. B* **2001**, *64*, 125102. [[CrossRef](#)]
113. Dall’Olio, S.; Dovesi, R.; Resta, R. Spontaneous polarization as a berry phase of the hartree-fock wave function: The case of KNbO₃. *Phys. Rev. B* **1997**, *56*, 10105–10114. [[CrossRef](#)]
114. Noel, Y.; Zicovich-Wilson, C.M.; Civalleri, B.; D’Arco, P.; Dovesi, R. Polarization properties of ZnO and BeO: An *ab initio* study through the berry phase and wannier functions approaches. *Phys. Rev. B* **2001**, *65*, 014111. [[CrossRef](#)]
115. Dovesi, R.; Pierre, M.D.L.; Ferrari, A.M.; Pascale, F.; Maschio, L.; Zicovich-Wilson, C.M. The IR vibrational properties of six members of the garnet family: A quantum mechanical *ab initio* study. *Am. Mineral.* **2011**, *96*, 1787–1798. [[CrossRef](#)]
116. Ferrari, A.M.; Valenzano, L.; Meyer, A.; Orlando, R.; Dovesi, R. Quantum-mechanical *ab initio* simulation of the raman and IR spectra of Fe₃Al₂Si₃O₁₂ almandine. *J. Phys. Chem. A* **2009**, *113*, 11289–11294. [[CrossRef](#)] [[PubMed](#)]
117. Maschio, L.; Ferrabone, M.; Meyer, A.; Garza, J.; Dovesi, R. The infrared spectrum of spessartine: An *ab initio* all electron simulation with five different functionals (LDA, PBE, PBESOL, B3LYP and PBE0). *Chem. Phys. Lett.* **2011**, *501*, 612–618. [[CrossRef](#)]
118. Deer, W.A.; Howie, R.A.; Zussman, J. *An Introduction to the Rock-Forming Minerals*, 2nd ed.; Longman: London, UK, 1992; 724p.
119. Chopelas, A. Single crystal raman spectra of forsterite, fayalite, and monticellite. *Am. Mineral.* **1991**, *76*, 1100–1109.
120. Hofmeister, A.M. Thermal conductivity of spinels and olivines from vibrational spectroscopy: Ambient conditions. *Am. Mineral.* **2001**, *86*, 1188–1208. [[CrossRef](#)]
121. Kolesov, B.A.; Geiger, C.A. A raman spectroscopic study of Fe–Mg olivines. *Phys. Chem. Miner.* **2004**, *31*, 142–154. [[CrossRef](#)]
122. Reynard, B. Single-crystal infrared reflectivity of pure Mg₂SiO₂ forsterite and (Mg_{0.86}, Fe_{0.14})₂SiO₄ olivine. *Phys. Chem. Miner.* **1991**, *18*, 19–25. [[CrossRef](#)]
123. Sogawa, H.; Koike, C.; Chihara, H.; Suto, H.; Tachibana, S.; Tsuchiyama, A.; Kozasa, T. Infrared reflection spectra of forsterite crystal. *Astron. Astrophys.* **2006**, *451*, 357–361. [[CrossRef](#)]
124. Suto, H.; Sogawa, H.; Tachibana, S.; Koike, C.; Karoji, H.; Tsuchiyama, A.; Chihara, H.; Mizutani, K.; Akedo, J.; Ogiso, K.; et al. Low-temperature single crystal reflection spectra of forsterite. *Mon. Not. R. Astron. Soc.* **2006**, *370*, 1599–1606. [[CrossRef](#)]
125. Navarro-Ruiz, J.; Ugliengo, P.; Rimola, A.; Sodupe, M. B3LYP periodic study of the physicochemical properties of the nonpolar (010) Mg-pure and Fe-containing olivine surfaces. *J. Phys. Chem. A* **2014**, *118*, 5866–5875. [[CrossRef](#)] [[PubMed](#)]
126. Wunder, B.; Jahn, S.; Koch-Müller, M.; Speziale, S. The 3.65 Å phase, MgSi(OH)₆: Structural insights from DFT-calculations and T-dependent IR spectroscopy. *Am. Mineral.* **2012**, *97*, 1043–1048. [[CrossRef](#)]
127. Yang, H.; Prewitt, C.T.; Frost, D.J. Crystal structure of the dense hydrous magnesium silicate, phase D. *Am. Mineral.* **1997**, *82*, 651–654. [[CrossRef](#)]

128. Frost, D.J.; Fei, Y. Stability of phase D at high pressure and high temperature. *J. Geophys. Res. Solid Earth* **1998**, *103*, 7463–7474. [[CrossRef](#)]
129. Hajilar, S.; Shafei, B.; Cheng, T.; Jaramillo-Botero, A. Reactive molecular dynamics simulations to understand mechanical response of thaumasite under temperature and strain rate effects. *J. Phys. Chem. A* **2017**, *121*, 4688–4697. [[CrossRef](#)] [[PubMed](#)]



© 2018 by the authors. Licensee MDPI, Basel, Switzerland. This article is an open access article distributed under the terms and conditions of the Creative Commons Attribution (CC BY) license (<http://creativecommons.org/licenses/by/4.0/>).